Multitemporal UAV Photogrammetry For Sandbank Morphological Change Analysis: Evaluations of Camera Calibration Methods, Co-Registration Strategies, and the Reconstructed DSMs

Ruli Andaru , Jiann-Yeou Rau, Laurence Zsu-Hsin Chuang, and Chia-Hung Jen

Abstract—Sandbank morphology is a longshore corridor with fast morphological changes. To analyze its changes, unmanned aerial vehicle (UAV) is the preferred effective and flexible data collection platform, which can collect very high resolution images. UAV campaigns along corridor areas require well-distributed ground control points (GCP) and accurate geotagged image positions to avoid misalignment errors of generated digital surface models (DSMs). However, a sandy terrain can make the measurement of GCPs difficult or even impossible. Furthermore, UAVs are often equipped with consumer-grade devices (onboard GNSS and nonmetric cameras), which, therefore, cannot provide accurate image positions and lead to geometric distortions of the image network due to inappropriate lens distortion corrections. This article proposes a strategy to calibrate the used camera and co-register multitemporal images without the need for accurate geotagged information on the whole datasets and well-distributed GCPs. The proposed strategy includes two improvements. First, we performed semi-on-the-job self-calibration (semi-OTJSC) using UAV images with favor orientations and flight altitudes to precalibrate interior orientation parameters (IOPs) and additional lens distortion parameters. This was then followed by another OTJSC of IOPs involving images with accurate geotagged positions. Second, a "transferred aerial-triangulation (Trans-AT)" strategy is proposed to co-register two consecutive UAV datasets through AT procedure similar to GNSS-supported AT within a strip image block. The experimental results revealed that the proposed method provides the best-fit camera parameters and generates high-accuracy co-registered DSMs. This strategy contributes significantly to multitemporal camera calibration and co-registration procedures for determining morphological changes in corridor mapping.

Ruli Andaru is with the Department of Geomatics, National Cheng Kung University, Tainan City 701, Taiwan, and also with the Department of Geodetic Engineering, Gadjah Mada University, Yogyakarta 55281, Indonesia (e-mail: ruliandaru@ugm.ac.id).

Jiann-Yeou Rau is with the Department of Geomatics, National Cheng Kung University, Tainan City 701, Taiwan (e-mail: jyrau@geomatics.ncku.edu.tw).

Laurence Zsu-Hsin Chuang is with the Institute of Ocean Technology and Marine Affairs, National Cheng Kung University, Tainan City 701, Taiwan (e-mail: zsuhsin@ncku.edu.tw).

Chia-Hung Jen is with the Department of Geography, CDTL, National Kaohsiung Normal University, Kaohsiung City 80201, Taiwan (e-mail: jen@nknu.edu.tw).

Index Terms—Images co-registration, multitemporal, sandbank corridor, transferred aerial triangulation (Trans-AT).

I. INTRODUCTION

A. Motivation

In coastal environments, sandbanks play a key role as protection against waves or tropical cyclone, sediment resources, and offshore wind farm deployments [1]. The existence of sandbanks is important because they can protect inlands and nearby coastlines [2]. Sandbanks' shapes and locations can change quickly due to sand migration that evolves under the effects of both natural coastal factors (ocean waves, tidal forces, wind, rainfall, and cyclones) and human influences. Many of them are subject to natural erosion, migration, and changes in morphologies [3], [4]. These changes can increase the risk of sediment imbalance and destabilize sandbank systems [5]. Therefore, periodic monitoring of its morphological changes is essential to investigate their stability in the coastal system.

Multitemporal morphological changes analysis can be characterized according to RGB orthoimages, co-registered point clouds, and successive digital terrain models (DTMs). The primary required data for this analysis includes a DTM because it represents the earth surface and can be used to analyze the morphological changes in the sequential dates. Since this mapping morphology requires repeated data collection, they should be applied in an effective, rapid, and low-cost manner with some convenient methods.

The morphological change parameters can be derived and analyzed from high-resolution stereo satellite images. However, satellite images have limitations for collecting geospatial data (particularly elevation data) at a specific time and location due to the orbit design [6]. For example, data collection over sandbank areas requires observations near the lowest tidal times to expose the largest sandy area. On the other hand, satellite images with in-track stereo pairs (such as IKONOS, Pleiades, SPOT-6, ALOS PRISM, and ZY-3) can extract high-quality digital surface models (DSMs) with vertical accuracies of 1.4–5 m [7]. However, they might not able to detect sandbank elevation changes with a sufficient degree of certainty (sand dunes have a rate of elevation

changes of approximately 0.8 m/year as reported by Mahmoud *et al.* [8] and Łabuz [9]).

Sandbank morphological mapping has also been collected through GNSS real-time kinematic (RTK) positioning [3], [4], total station, and mobile laser scanning [10]. However, a long corridor coastal area causes inefficient data acquisition, which is also labor-intensive, and infeasible to be carried out on site correspondingly. Meanwhile, sandbank mapping based on airborne laser scanning (ALS) survey is also relevant to this study [11], [12]. ALS itself is the most accurate active sensor technology for producing high-density point clouds with a large coverage. It can produce a smooth bare earth elevation model even on sandbank areas which are partly vegetated because the ALS sensor is able to pass through the gap of leaves. However, it requires a relatively expensive laser transmitter/receiver and complicated hardware to be mounted in the aircraft [13] as well as accurate boresight calibration among sensors. Another type of aerial mapping, i.e., airborne photogrammetry is also applicable to this study. Nevertheless, the aircraft services are less flexible when operated at a specific time and in a small-scale coverage area.

B. UAV Potential, Problems, and Challenges

Unmanned aerial vehicle (UAV) remote sensing offers new opportunities for scale-appropriate measurements of corridor-shaped study areas such as road and river landscapes [14], [15], power line design [16], and dune systems [10]. UAV utilization for mapping purpose has recently emerged since it offers operational flexibility, high spatial and temporal resolutions, and low-cost budget with acceptable accuracy [1], [17]. In particular, to map sandbank morphologies, the common photogrammetry structure-from-motion multiview stereo (SfM-MVS) algorithm can be applied [18]. However, in low-contrast regions (e.g., flat sandy and water areas), the tie-point extractor in the SfM processing chain easily fail to identify the conjugate features [19]. The homogeneous and low-textured surface introduces uncertainty while extracting the feature descriptors in the image matching process, leading to insufficient matched tie-points and uneven spatial distribution [20].

Another limitation concerning UAV photogrammetry in corridor mapping is that it generally has weak imaging geometry toward inaccurate and deformed 3-D surface reconstruction. As summarized in [21] and [22], this weak geometry is typically caused by the following:

1) a near-parallel or long strip flight configuration, which leads to a weaker image network;
2) narrow field of view of the used camera/lens, which in turn leads to a poor intersection angle of corresponding points;
3) a less convergent angle camera configuration, which decreases the base-to-depth (B/D) ratio;
4) an insufficient number and uneven spatial distribution of ground control points (GCPs);
5) inaccurate measurement and poor spatial distribution of tie-points, resulting in inaccurate and unreliable relative orientation.

To map the corridor shape, a UAV campaign acquires images through a linear round-trip configuration [23]. In recent decades,

UAVs are equipped with consumer-grade cameras that are usually smaller, lighter, and cheaper than survey-grade sensors (e.g., a metric camera). Consumer-grade cameras are not dedicated for mapping purposes due to their unstable internal geometry with lens distortion, which can introduce many systematic errors that cannot be completely corrected. As reported in [21] and [24], an inappropriate camera calibration method or incomplete lens distortion correction in corridor mapping missions will introduce geometrical deformations (e.g., "bowl or banana" effects) in the imaging network and produces deformed DSMs. These effects can be reduced through several strategies, e.g., increasing the number of GCPs with even distribution, adopting flight missions at different altitudes with large convergent view angles through vertical/oblique images or incorporating the measurement of exterior orientation parameters (EOPs) by utilizing high-end inertial navigation system fused with post processed kinematic GNSS (PPK) through direct georeferencing technique [10], [25], [26]. However, due to the nature of sandbank corridor, implementing those strategies are often unavailable because of several reasons, which are as follow.

1) For a large sandbank area, measuring GCPs with RTK are time-consuming and sometimes impossible because of their inaccessibility.
2) The consumer/commercial-grade UAVs are often equipped with an onboard GNSS (GNSSNAV) sensor for geotagging image positions. Even though cheap and light RTK/PPK GNSS modules have recently been available and can be installed on small UAVs, their accuracy and reliability, however, remain poorly quantified [27].
3) Adopting flight missions with convergent viewing angles (e.g., acquiring both vertical and oblique images) can strengthen the imaging network. However, it will increase the total number of flights and image acquisition time, which definitely causes the sandbanks to be photographed at different tidal elevations.
4) In case of carrying multiple digital cameras with different view angles, the total weight of payload will be increased, thereby reducing the overall endurance time and travel distance.

In order to analyze time-series data and minimize errors associated with misalignment at the same areas captured on different dates, multitemporal UAV datasets need to have a consistent reference frame and are geometrically co-registered. Several methods are introduced in both the fields of image-based registration and cloud-based registration. For example, Feurer and Vinatier [28] integrated multiepoch images within a single block through SfM algorithm to compute key points among all epochs and then calibrated IOPs and EOPs simultaneously. Aicardi *et al.* [29] presented co-registration of two datasets using a reference image blocks co-registration algorithm. Zambanini [30] introduced registration approach through a Hough Voting mechanism that transfers the local feature correspondences to the probabilities of geometrical relationships between images. Image-based registration was also suggested by Nagarajan and Schenk [31] to co-register historical aerial images on the basis of unchanged linear features. A similar approach was described by Zhao and Goshtasby [32] as well through a homographic

transformation (i.e., 2-D projective transformation) for registration of various aerial images. In addition, multitemporal co-registration can also be applied through 3-D point clouds registration. After 3-D point cloud from images have been obtained, then two time-series point cloud can be registered. The most popular algorithm in practical automatic pipelines is iterative closest point [33] with their variants, such as sparse closest point [34] and geometric primitive closest point [35]. However, cloud-based registration is not appropriate for co-registering sandbank objects, as it requires significant geometrical object variation.

Regarding the camera calibration method in a corridor UAV mapping, Jaud *et al.* [26] proposed a new camera model to minimize "bowl effect." The model consists of two calibration layers, i.e., extra polynomial coefficients and nonradial degree 7 polynomial correction to rectify the remaining deformations. Although this camera model can limit DSM's bowl effect, the inclusion of oblique images together with images in varying altitudes were still required.

The above-cited papers mainly involve few optical images with image block configurations or shorter corridor shapes. The tested images also have sufficient obvious intensity variations for feature points extraction and matching. In contrast, the datasets used in this article are in a long corridor shape which spreads for 1 km by 30 km along the coastal area, where is dominated by water body and sand with poor intensity variations. The image-based 3-D reconstruction technique on the large open water bodies also causes noises in the generated depth maps due to matching ambiguities, which were mainly caused by wave fluctuations, poor image texture, and sunlight reflections. Consequently, extremely noisy points were present in the produced dense point clouds [36], [37]. Thus, it is also essential to classify and remove these noisy points prior to the DSM generation.

C. Objectives

This study demonstrates the use of SfM-MVS photogrammetry for sandbank morphological changes analysis through multitemporal UAV images. As described earlier, several factors may lead to deformation in the generated DSMs; they are summarized as follows:

1) Geometric distortion of the images network due to an inappropriate calibrated camera model together with a linear image strip configuration that has a weak imaging geometry. To eliminate this problem, a new strategy of camera calibration with a semi-on-the-job self-calibration (semi-OTJSC) is proposed.

2) Improper co-registration of multitemporal UAV products because the measurements of well-distributed GCPs and accurate geotagged images are not all available. To deal with this limitation, a co-registration procedure, i.e., transferred aerial-triangulation (Trans-AT) is introduced.

3) Image matching uncertainty due to insufficient distinct key-point and their spatial distribution in the image frame, mainly on low-textured surfaces. Here, we propose the use of contrast limited adaptive histogram equalization (CLAHE) image enhancement [38].
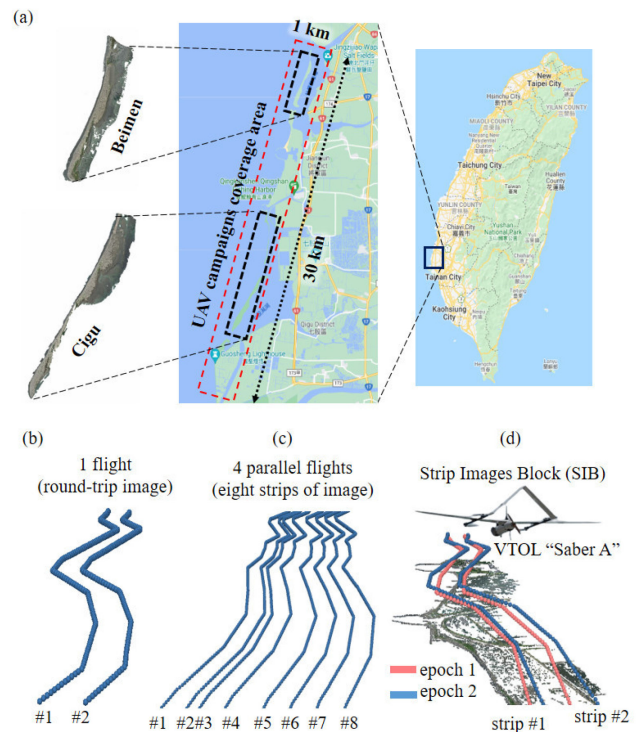

Fig. 1. (a) Location of the study site of two sandbanks on the southwestern coast of Taiwan (denoted within the black square of the map on the right). The red and black dotted rectangles denote UAV image coverage and two sandbanks, respectively. (b) UAV campaign configuration over sandbank areas. Each UAV flight contains a round-trip image. (c) T6 and T7 datasets each contain four flights, making eight parallel strips of image. (d) Configuration of a strip image block (SIB) that consists of two consecutive datasets.

4) The presence of noise points among the generated dense point clouds due to image matching failure, which mainly occurs in the area of water bodies. To remove these noises, a supervised machine learning algorithm, random forest is adopted [39].

II. DATA AND WORKFLOW

A. UAV Campaigns

The datasets for sandbank morphological changes analysis were obtained from eight UAV campaigns in 2019–2020 (see Table I) at southwestern Taiwan where two sandbanks (Cigu and Beimen) were chosen as study sites [see Fig. 1(a)]. A vertical take-off and landing UAV called "Saber-A" [see Fig. 1(d)] equipped with a Sony A7r2 camera and a 15 mm prime lens was used for aerial image acquisition. This lens was chosen because it has a wide field of view of 110° as well as small lens distortion, which is capable of increasing the geometric strength and positional accuracy, particularly in the vertical direction, and is beneficial for gentle terrain surface reconstruction.

The UAV campaigns photographed a 1 km × 30 km corridor-shaped area, covering 10 km × 0.5 km of Cigu and 4.2 km × 0.5 km of Beimen sandbanks at a flight altitude of 400 m [see Fig. 1(a)]. To increase the geotagged image positional accuracy, we installed a PPK module on the UAV; however,

TABLE I
UAV SURVEYS OF THE SANDBANK AREA

EPOCH TIME	T1	T2	T3	T4	T5	T6 *	T7	T8
YEAR	2019	2019	2019	2019	2019	2020	2020	2020
Acquisition date	April 20	May 19	July 4	July 17	August 31	April 10	July 5	October 16
Acquisition time								
• Start mission	4.20 PM	4.20 PM	4.40 PM	4.33 PM	4.28 PM	10.02 AM	10.21 AM	4.03 PM
• End mission	5.20 PM	5.25 PM	5.50 PM	5.40 PM	5.29 PM	5.23 PM	5.10 PM	4.35 PM
Number of flight mission	One flight (two strips)					Four parallel flights (eight strips)		One flight (two strips)
Lowest tidal time	4:41 PM	4:32 PM	5:24 PM	4:47 PM	4:40 PM	5:35 PM	4:34 PM	3:19 PM
Images number #	957	959	777	982	1100	1118	1012	447

Note: *Dataset containing accurate geotagged positions through the PPK technique.

it did not work stably and most of them failed during flights for unknown reasons. The only successful collection of PPK for in-flight positions was available on the T6 dataset. We have estimated that the image positional errors provided by the PPK module were approximately 20 and 25 cm for horizontal and vertical directions, respectively. These errors were estimated by performing bundle adjustment that involves 31 GCPs to compute the optimized EOPs. Prior to the bundle adjustment, we set up the *a priori* standard error of camera's initial positions with a lower weight. The root mean square error (RMSE) between the adjusted image positions and PPK geotagged coordinates represents the PPK geotagged positional error. Additional geotagged information was provided by the GNSSNAV system, which has approximately 5 m geolocation accuracy.

In general, the UAV flight plan for corridor mapping was set with a round-trip, i.e., the traveling and returning strips, as illustrated in Fig. 1(b). With a mapping area of 1 km × 30 km, Saber-A needs to fly for roughly an hour and obtain a trajectory of approximately 70 km for each flight. In particular, for the T6 and T7 epochs, we acquired four flights of UAV images, i.e., eight parallel strips in total as illustrated in Fig. 1(c). This provides a total swath width of about 3 km. All UAV campaigns were able to acquire the two sandbanks completely except the T8 because a strong wind occurred during the flight mission. Consequently, the T8 mission only covers Cigu sandbank. For all UAV campaigns, the aerial photographs were acquired at a flight altitude of 400 m with a 60% side lap and 90% forward overlap.

According to the used camera, which has a pixel size of 4.5 μm, it can provide very high resolution images with a spatial resolution that is 12 cm. The flexibility of UAV deployment allows us to set up the acquisition within the lowest tide period. According to the tidal forecast (https://www.cwb.gov.tw), the lowest tidal time generally occurs in the late afternoon (see Table I), which also has the benefit of reducing the Sun's reflection from the water body.

B. GNSS in Situ Surveying

The objectives of GNSS surveying are to measure GCPs (used within AT for georeferencing) and independent check points (ICPs), which are used to estimate the accuracy after AT. Due to

the rapid natural change of the sandbank surface and its inaccessibility, we could only measure GCPs/ICPs at the inland areas. We have collected 20 GCPs and 11 ICPs measured by the virtual base station real-time kinematic (VBS-RTK) GNSS, a method formulated by the National Land Surveying and Mapping Center, Taiwan (https://egnss.nlsc.gov.tw). They were spread over three inland areas along the 30 km corridor of the study area, as shown in the red rectangles in Fig. 2. However, their positions were unevenly distributed. The placement and measurement of GCPs at both sandbanks were unfortunately unavailable. For the accuracy assessment of co-registration and vertical discrepancies over the sand surface, two elevation profiles were measured using the VBS-RTK (blue rectangle in Fig. 2). However, these data were only available on the T8 dataset and were measured at one day before the UAV mission. Three additional surface profiles were also observed as ground truth in the inland areas (yellow rectangle in Fig. 2).

C. CLAHE Image Enhancement

Before the semi-OTJSC and the Trans-AT process, we applied CLAHE enhancement for the whole UAV image datasets in order to increase the number of detected feature points and improve the AT reliability and accuracy. The CLAHE enhancement is a refinement of the adaptive histogram equalization algorithm proposed by Pizer *et al.* [38] to improve the local image contrast. It presents two parameters to control enhanced image quality: tile size and clip limit. The larger clip limit, the higher contrast and brightness of the enhanced images. If some grey levels in the image exceed the clip limit threshold, the excess is evenly distributed to all the grey levels.

As a result, the enhanced image will not be over-contrast or saturated, and the noise amplification can be reduced as well. The contrast can also be controlled by setting the tile size. The enhanced images become higher contrast when the tile size is set to a larger value as the dynamic range becomes larger [40]. Previous studies describe that the CLAHE algorithm significantly improved visual image quality, increased numbers of tie-points and dense point clouds, and reduced noise [41], [42]. The enhanced images were then used to align photos and generate 3-D dense point clouds, DSMs, and orthoimages of the sandbank area.
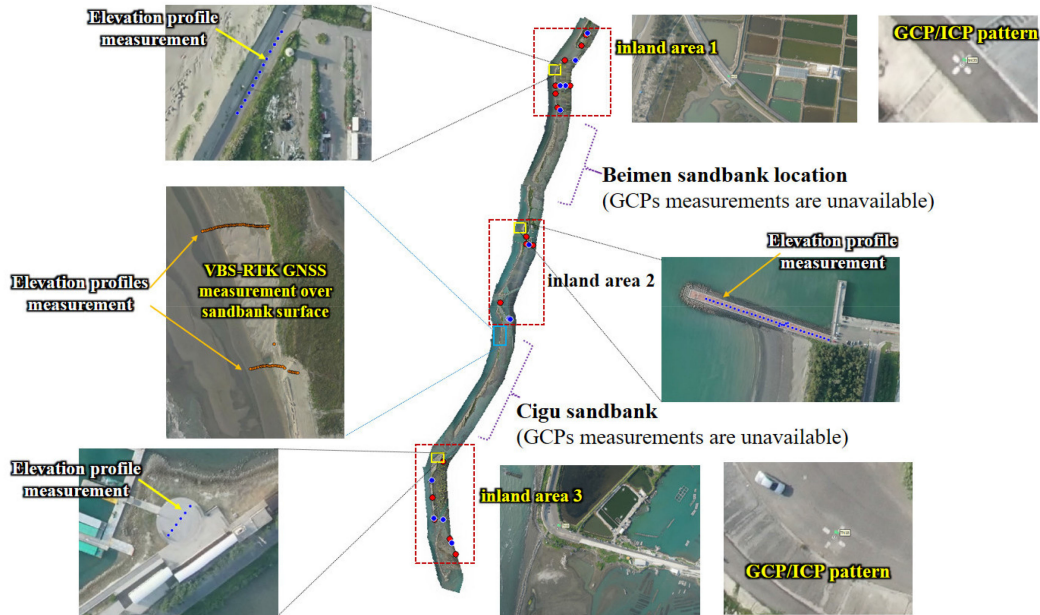
Fig. 2. Distribution of GCPs (red dots) and ICPs (blue dots) along two sandbanks. The red dotted rectangles indicate the GCPs/ICPs positions in three inland areas. Enlarged images: the light blue rectangle depicts the measurement of elevation profiles on the date of T8 over Cigu sandbank while the yellow rectangles depict the measurement of elevation profiles at three inland areas. All GCPs and ICPs are located and painted (with white cross patterns) on stable surfaces, such as road, embankment, and pavement.

D. Proposed Strategies

Fig. 3 shows the workflow of this study which generally exploits photogrammetric algorithms to perform the camera calibration, co-registration, and generated DSMs together with orthoimages. Agisoft Metashape Pro software was chosen for those tasks. This section introduces detailed descriptions of the two improvements. First, a "semi-OTJSC" is proposed for camera calibration that contains two steps procedures. Second, a method to co-register two consecutive UAV datasets called "Trans-AT" is proposed. The two consecutive datasets were aligned within a single strip image block (SIB) through the AT process. The configuration of SIB is depicted in Fig. 1(d) which consists of two consecutive datasets. Each dataset represents one epoch date and contains of two strip images. The main goal of "Trans-AT" is to co-register time-series datasets successively within an SIB that allows the reference dataset act as "aerial control" to constrain the trajectory of the other dataset within the SIB.

The accuracy assessment of the proposed multitemporal co-registration was evaluated using VBS-RTK GNSS measurement over the sandbank surface and several unchanged inland areas. Another two different co-registration strategies, i.e., "independent AT with OTJSC" and "AT by joining multi-epochs into a single block," have also been compared to assess their effectiveness and absolute positional accuracy. In addition, three camera calibration methods were compared: OTJSC using images acquired from sandbank UAV mission, precalibration using image with Australis retro-coded targets acquired at an indoor calibration field (PC1-indoor), and precalibration using terrestrial images acquired in front of a tall building (PC2-outdoor).

1) *Semi-OTJSC:* The nonmetric cameras employed in UAVs generally exhibit unstable IOPs; therefore, their internal geometry might change over time [43]. The used camera in this work is indeed considered a professional or high-end consumer grade digital camera that has several features such as robust structure and full-frame CMOS sensor with high resolution and sensitivity. In order to evaluate the stability of internal camera geometry, we performed a stability test by calculating the change significance index as described by Rau and Yeh [44]. Here, only focal length and two lens distortions (i.e., radial and tangential distortions) were evaluated. The change significance's plot is shown in Fig. 4, calculated from four time-series image datasets (D1–D2, acquired in 2019, and D3–D4 acquired in 2020). As a result, six change significance indexes (c) between two epochs could be obtained. It can be seen that the focal length tends to be stable (c values are smaller than a prespecified threshold, e.g., < 50), which is in accordance with the prime lens used in this work. In addition, the tangential distortions are considered stable as well. Meanwhile, the c values of radial distortions are higher than the threshold which means that the radial distortions are likely to be unstable over time. Since the radial distortions are the main geometric distortion in raw imagery and its magnitudes are up to hundreds of pixels compared with the tangential ones (typically are less than 0.5 pixels) [45], therefore in the stability analysis for lens distortion, we only considered the significance test results of radial distortions.

Based on these test results, we consider separating the camera's internal geometry into two parts, i.e., IOPs (focal length and principal points offset) and additional lens distortion parameters (APs). In which, APs comprise three radial distortion coefficients (k1, k2, k3), two tangential distortion coefficients (p1, p2), and two parameters to account for affinity and skewness
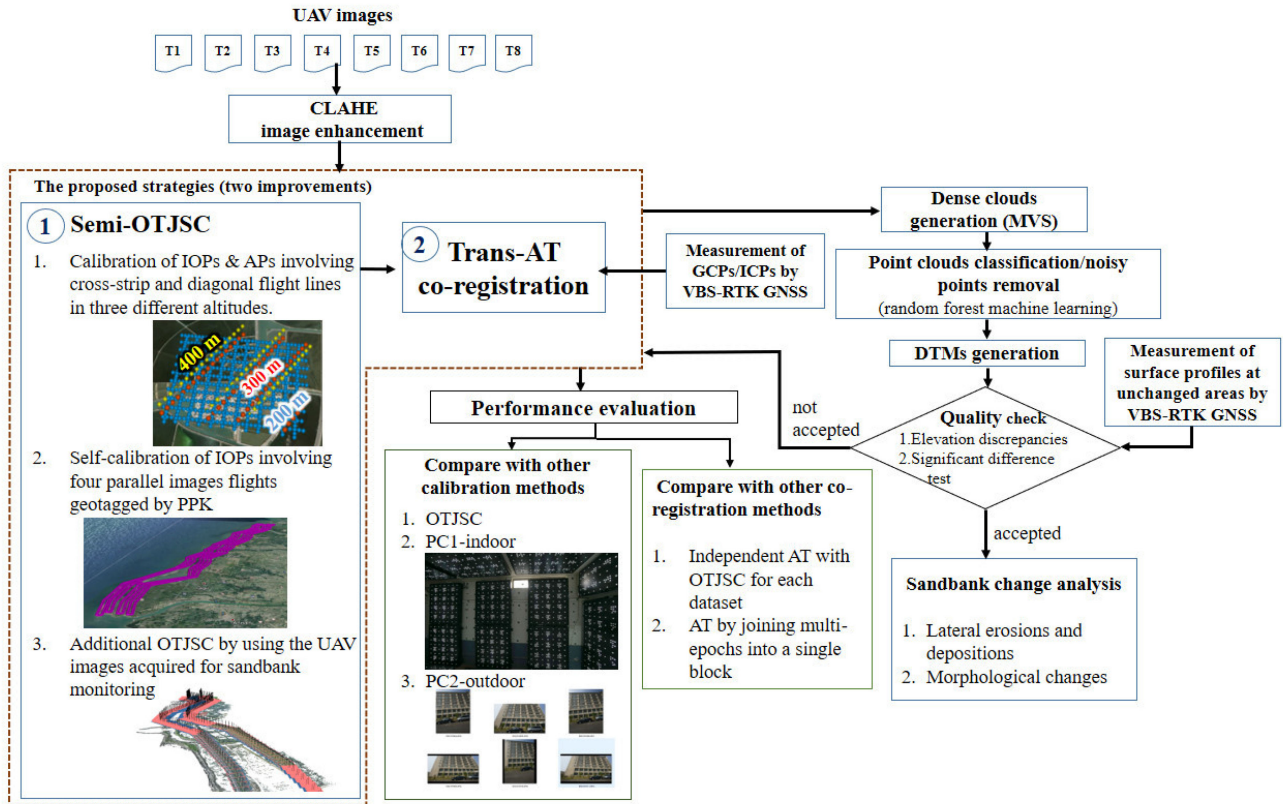
Fig. 3. Workflows of the proposed method (two improvements), the performance evaluation, and the change analysis.
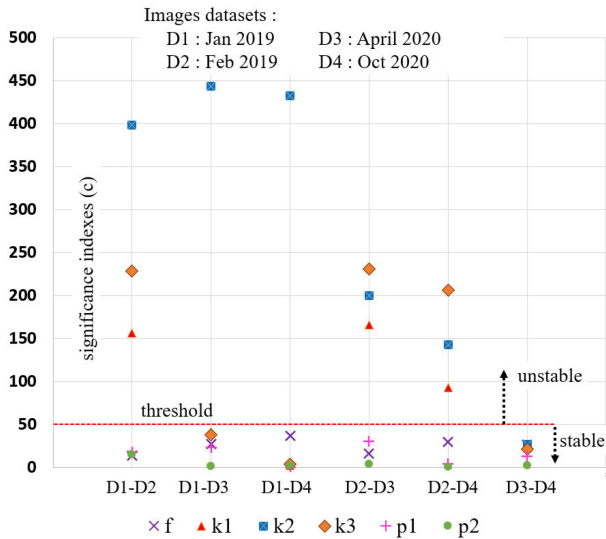

Fig. 4. Stability analysis of the used lens/camera in two years from four time-series datasets.

TABLE II
UAV DATASETS FOR CAMERA CALIBRATION

Dataset	Configurations	Altitude	Images #
1 Non-mission UAV sandbank	• Rectangular image block with cross-strip flight lines (Fig. 3) • Geotagged image position by onboard GNSSNAV	Different altitudes : 200 m, 300 m, and 400 m	740
2 UAV mission (T6 dataset)	• Four parallel flights (Fig. 3) • Geotagged image position by PPK	400 m	4,500

(b1, b2). Considering the image configurations of our datasets for the camera calibration process, we proposed a two-step "semi-OTJSC" procedure involving datasets #1 and #2 for pre-calibration (the details of their configurations are described in Table II). It was then followed by an additional OTJSC using the UAV mission for each epoch dataset.

The main purpose to involve images with varying configurations is to obtain an appropriate IOPs for all eight epochs. Adopting image sets with different altitudes will reduce projective coupling between IOPs and EOPs and exhibit negligible DSM deformation [46], [47]. Additionally, the correlation between focal length and flight height can also be decoupled by adopting flight in different altitudes as well as using PPK for height constraint [46], [48]. Here, we performed these calibration procedures through self-calibration bundle adjustment (SCBA), which is typically used in SfM-based alignment. In order to constrain object and camera space in the BA process, it is important to incorporate a set of GCPs and high-accuracy geotagged images positions during SCBA [46], [49]. The two-step "semi-OTJSC"
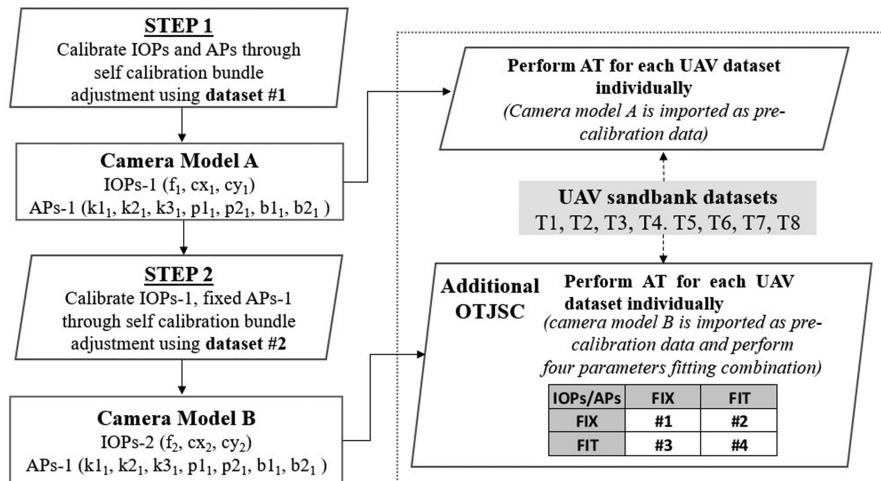
Fig. 5.   Proposed semi-OTJSC steps.

procedures are shown in Fig. 5 in detail which comprises several steps as follows.

1) Perform SCBA, which involves images in dataset#1 and six GCPs resulting in IOPs-1 and APs-1.

2) Import those IOPs-1 and APs-1 as initial values for the second step of SCBA (incorporating 65 GCPs) by using dataset#2. Suppose incorporating the PPK positions in dataset#2 can decouple the correlation between the focal length and flight altitude by means of using altitude constraint, in this step, only IOPs-1 were calibrated (fit IOPs). Another consideration to only calibrating IOPs-1 is that the APs-1 are more reliable due to the images in dataset #1 have strong imaging geometry with varied image configurations. As a result, the IOPs-1 were adjusted (resulting in IOPs-2) and APs-1 were kept.

3) In the final step, additional OTJSC was performed using the UAV sandbank images. Since the used nonmetric camera generally exhibits unstable internal geometry over time, we needed to investigate the parameter-fitting combination between IOPs and APs. There are four parameter-fitting combinations involving IOPs-2 and APs-1 needed to be evaluated in advance:

   a) fix both IOPs and APs;
   b) fix IOPs-Fit APs;
   c) fit IOPs-Fix APs;
   d) fit both IOPs and APs.

   The best one with the highest accuracy is considered the best-fit calibration model.

2) Trans-AT Co-Registration: In this section, we present a multitemporal UAV images co-registration strategy based on the positional information obtained from the reference SIB to constrain the initial positions of the following SIB through a GNSS-supported AT procedure. For simplicity, in the remainder of this article, the term GNSS-supported AT is expressed as "AT." The Trans-AT is a dependent AT procedure, meaning that the two image datasets (which are taken at different dates) are aligned together at the same time; one as the reference and the other one as the target. Here, the corresponding points (tie-points)

between those two epochs are required and used for constraining to each other depending on whose initial positions' weight is higher.

The observation equations of GNSS-supported AT contain the observed coordinates of the camera perspective center (observed with in-flight positions by PPK/GNSSNAV), the observed image coordinates of tie-points, the field-surveyed GCPs coordinates, and the unknown rotational angles of each camera (ω, φ, κ). The GNSS-supported AT uses the least-squares to estimate the camera positions and orientations, tie-points' 3-D coordinates, and optional IOPs and APs. Similar to the AT procedure in traditional photogrammetry, the SfM implements AT in three stages [50]. First, the relative orientation parameters (ROPs) are estimated using tie-points observations between image pairs. These ROPs can be mathematically determined with collinearity or co-planarity equations. In SfM photogrammetry, when calibrated images are used, the ROPs can be computed by decomposing the Essential Matrix (the set of linear homogeneous equations that are formed by establishing eight-point correspondences) [51]. The second step is establishing a reference coordinates system for deriving the EOPs and tie-points' 3-D coordinates. The most common approach to obtain the EOPs in SfM commercial software is to use an incremental strategy through an image augmentation process, such as direct linear transform inside random sample consensus procedure [50]. At the final step, a bundle adjustment procedure is implemented to adjust and optimize the EOPs and all tie-points' 3-D coordinates obtained at the second stage. It is also able to integrate ICPs at this stage, which, therefore, can be used for AT accuracy analysis.

Through tie-point observations between image pairs, the GNSS-supported AT based SfM framework can solve the ROPs as well as estimate EOPs of all involved images which refers to a mapping frame without incorporating any GCPs. However, several studies recommended incorporating GCPs in the bundle adjustment (even only one GCP) to reduce elevation biases [52], [53]. The quantity of GCPs is, indeed, directly related to the number of observations and can be used as a constraint in the
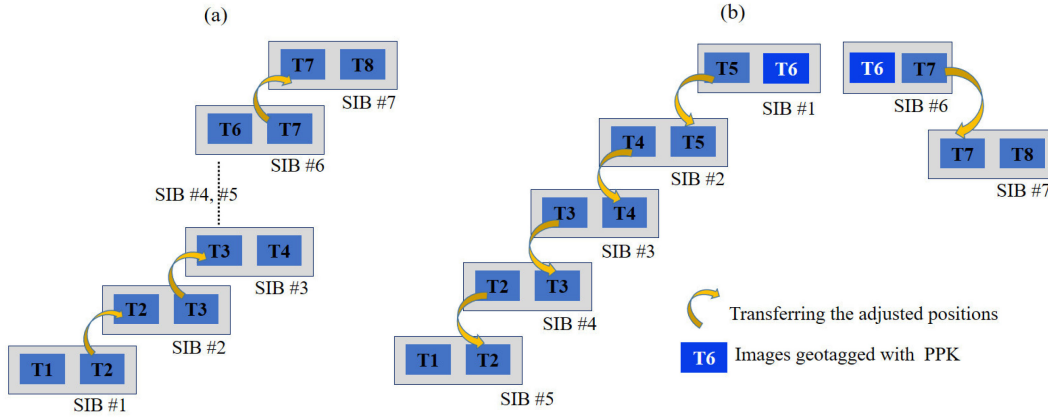
Fig. 6. (a) Basic concept of Trans-AT co-registration procedure involving eight epochs of UAV images datasets. (b) Modified Trans-AT co-registration procedure. It starts from the T6 dataset (considered as the reference) due to T6 having accurate geotagged image positions provided by PPK.

least-squares adjustment. As a constraint, GCPs are treated to the higher weight according to the estimated uncertainty associated with the field survey methods. Thus, more GCPs will lead to a more reliable bundle adjustment [53].

Because the images on all datasets (except for T6) do not have PPK in-flight positions, we used onboard GNSSNAV instead with the help of several GCPs in the inland areas. To constrain the initial positions of the following SIB, the positional information from the common dataset of two consecutive SIBs was transferred from the former to the latter. This procedure considers the first SIB (SIB #1) as the reference one and is used to constrain the latter one sequentially [see Fig. 6(a)]. For more details, the Trans-AT co-registration steps are described as follows.

1) Combine images of T1 and T2 datasets into one block (SIB #1) and perform the AT process together with several GCPs. In total, 20 GCPs and 11 ICPs were used (their distribution is shown in Fig. 2).
2) Export the EOPs of T2 (obtained from step 1). They were then imported into SIB #2 (includes T2 and T3). According to our previous experiments, unfixing the camera orientations will insignificantly affect the results (the rotation angles errors are, in fact, approximately 0.02˚). Thus, here only the positions were assigned with a small *a priori* standard error (e.g., 25 cm, see Section II-A). T2 is the common dataset of the SIB #1 and SIB #2, which was considered as aerial control for the alignment of SIB #2.
3) Perform AT of the SIB #2 with the same GCPs.
4) Repeat the same procedure from SIB #3 to SIB #7. In total, seven steps of Trans-AT were required to co-register all eight image datasets.

In the Trans-AT co-registration, the T1 of SIB #1 require accurate image positions because it is used as aerial control to constrain the following SIB. Inaccurate image positions of the reference dataset would introduce a systematic error and propagate to the following SIB. Owing to the T6 is the most accurate geotagged image positions, the Trans-AT sequence procedures need to be modified. It starts from T6 (considered as reference) to constrain the former and latter datasets. Despite

T6 and T7 have four parallel strips of images, we only consider two strips of images (strip #1 and #2) during the Trans-AT process (considering that general UAV mission conduct only one flight). The details of these procedures are shown in Fig. 6(b). It starts with conducting AT of the SIB #1 (T5 and T6). Then, the positions of T5 were transferred to the previous dataset (SIB #2). The same procedures were applied to the backward epochs (T4, T3, T2, and T1) by conducting AT of SIB #3, SIB #4, and SIB #5, as shown in Fig. 6(b). For the co-registration of the T8 dataset, the T6 dataset was used again as the reference for AT process of SIB #6 and SIB #7. This modification, therefore, implies the flexibility of the Trans-AT co-registration (i.e., the reference dataset does not necessarily correspond to the first epoch).

The presented co-registration method involves several GCPs during the registration process. These procedures not only solve the relative transformation between two consecutive epochs, but also adjust the mapping coordinate system to the absolute geographic location within the mapping datum accordingly. We also involved several ICPs on every Trans-AT step to examine the AT accuracy. In addition, to evaluate the Trans-AT co-registration results, we generated dense point clouds and DSMs then compared with the elevation profiles that were measured by VBS-RTK surveying in the inland areas (see Fig. 2).

E. Point Clouds Classification

SfM-MVS photogrammetry provides high-density 3-D point clouds, leading to a fine reconstruction of the topography [54]. However, the existence of water body areas surrounding sandbanks present noises in the generated dense point clouds. In addition, some parts of the sandbank areas were covered by vegetation and artificial objects, which result in a challenge for extracting bare sand surface. As a consequence, it is necessary to remove noises and filter nonsand objects. Our goal is to implement an efficient and robust approach for cleaning those nonsand point clouds. For this purpose, random forest was adopted. It is preferred because random forest was designed

to deal with large datasets and provide a fast point clouds classification. Moreover, it is regarded as a considerable supervised point clouds classification with a few training samples [39]. We adopted the random forest that was implemented in the LiDAR 360 version 4.0. The obtained bare-sand point clouds were then adopted to create DTMs with an equal grid size of 0.5 m.

F. Evaluation of Co-Registration Error

We evaluate the errors associated with co-registration misalignment with two different metrics. The first metric is the RMSEs of the GCPs/ICPs on each SIB after the AT process. The GCPs RMSE represents the internal accuracy of the whole imaging network after AT, while the ICPs RMSE denotes the absolute positional accuracy of check points that were not involved during the AT. In the second metric, we compared the elevation from the generated DTMs after co-registration by the VBS-RTK measurements on several unchanged areas. The elevation of these areas should be close to the elevation measured by VBS-RTK. We then assess the misalignment error through a significance test procedure. The Student's t-test with a desired significance level ($\alpha = 0.05$) is adopted, as depicted in the following [55]:

$$t = \frac{\bar{x} - \mu_0}{\sigma/\sqrt{n}} \qquad (1)$$

where t is the significance index at the level of significance α with a degree of freedom v, and $\bar{x}$ is the mean of the estimated parameter (i.e., vertical discrepancies between the generated DTMs and the VBS-RTK measurements). The true value of the parameter is expressed with μ_0. Meanwhile, σ is the standard deviation of the height difference, and n is the number of observations. The tested parameter is determined to be insignificantly different from the reference value if $t_{\text{value}} \leq t_{\text{table}}$.

G. Analysis of Morphological Changes

The complete set of well-registered and noise-free dense point clouds was obtained after the Trans-AT co-registration and point cloud classification. To investigate the morphological changes of sandbank surface quantitatively, we calculate the DTM difference between two successive datasets. This is typically conducted by subtracting the older DTM from the more recent one through a pixel-by-pixel calculation. Here, these changes were calculated in the overlapped areas of two successive DTMs. The result of DTM difference is a differential surface, which is a measure of the spatial distribution of the mass displacement [56].

III. Results and Discussions

The experimental results of the proposed two improvements are presented in this section. In Section III-A, we discuss the semi-OTJSC result, including the evaluation camera models A and B. The best-fit camera model obtained from the semi-OTJSC was then compared with other calibration methods (was evaluated through image residual and vertical discrepancies). Section III-B discusses the CLAHE performance for increasing the

number of valid matched points. The Trans-AT co-registration is discussed in Section III-C, including the comparison with other co-registration strategies. Because this comparison involves the generated DTMs, the bare-sand point clouds extracted by random forest machine learning were also analyzed and discussed in this section. Finally, the sandbank morphological change analysis is described in Section III-D.

A. Semi-OTJSC Camera Calibration

Based on the camera calibration method introduced in Section II-D1, two camera models were obtained: 1) camera model A, with IOPs-1 and APs-1 obtained from the first step, and 2) camera model B, with IOPs-2 and APs-1 obtained from the second step.

1) Evaluation of Camera Model A: In the beginning, we assess the stability and accuracy of camera model A for the entire eight datasets. The camera model A was fixed as precalibration data and then perform AT for each UAV dataset individually. Several GCPs/ICPs at each dataset were adopted, and the vertical RMSEs of ICPs were used to present the overall accuracy. Experimental results show the vertical RMSEs ranging from 9 to 29 cm [as shown in the cyan graphical bars in Fig. 7(a)] with an average of 15.7 cm. We further evaluate the absolute accuracy of the generated DTMs at sandbank surface (using T8 dataset) by comparing it with an elevation profile measured by VBS-RTK [as depicted in the cyan line in Fig. 7(b)]. This results in an average vertical error of 89 cm and vertical RMSE of 123 cm. Accordingly, these results demonstrate that camera model A is not appropriate and not stable to model the used lens/camera over all eight datasets.

2) Evaluation of Camera Model B: Camera model B was evaluated through the suggested semi-OTJSC calibration approach by implementing four parameter-fitting combinations. These combinations are suggested in the proposed camera calibration workflow in response to the fact that calibrating a nonmetric camera with the same IOPs and APs may not achieve the most appropriate camera model. Therefore, one of them may need to be self-calibrated by the UAV mission acquired images. The first combination "(1) Fix both IOPs and APs" is indeed the precalibration result of camera model B without OTJSC. This means that IOPs-2 and APs-1 were imported into all eight datasets individually and fixed during the AT process, while the other three combinations, (2)–(4), are calibrating one of the two parameters (IOPs or APs) or even both through OTJSC.

As shown in the vertical RMSEs of ICPs in Fig. 7(a), the two parameter-fitting combinations with "Fixed APs", i.e., combinations (1) and (3), during the AT process have introduced larger variations and errors [i.e., the green and brown graphical bars in Fig. 7(a)], particularly at three datasets (i.e., T1, T7, and T8). On the contrary, calibrating only the APs, i.e., combinations (2) and (4), tends to result in smaller errors [i.e., the pink and blue graphical bars in Fig. 7(a)]. These two combinations significantly reduce the error, particularly in those three datasets (i.e., T1, T7, and T8) mentioned above.
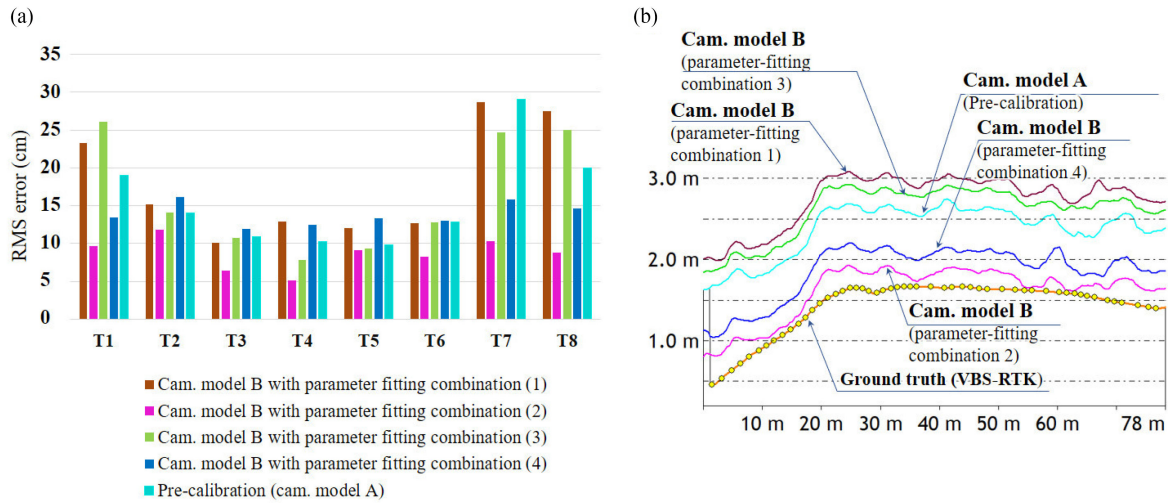
Fig. 7. Evaluation of the suitability of camera model A and B over eight datasets. (a) Vertical RMSEs of ICPs resulted from AT by implementing camera model A as precalibration and camera model B with four parameter-fitting combinations. (b) Elevation profile comparisons among the interpolated DTM elevation profiles by each camera model and the one measured by VBS-RTK over sandbank.

In detail, as shown in the brown graphical bars of Fig. 7(a), the corresponding vertical RMSEs of combination (1) has larger variation and appear higher errors with an average of 18 cm. While the combinations (3) and (4) have yielded high error as well, with the vertical RMSEs of 16 and 14 cm, respectively. On the other hand, the combination (2) has obtained the lowest error [as illustrated in the pink graphical bars in Fig. 7(a)], with an average vertical RMSE of 9 cm. Comparing these four combination results, it demonstrates that the combinations (1), (3), and (4) are not appropriate enough to model the internal geometry of the used camera/lens. Apart from that, by implementing the proposed semi-OTJSC approach with parameter-fitting combination (2), we can obtain the most appropriate and stable calibration results over the acquired time-series UAV images that have weak imaging network.

To further reconfirm the proposed semi-OTJSC procedure, we evaluate the absolute accuracy of the interpolated DSM elevation profiles on the sandbank surface by using all four combinations, but only applied to T8 dataset, which has the elevation profile ground truth measured by VBS-RTK. The results describe that the surface profile interpolated from the DSM with the combination (2) is the closest one to the ground truth [as depicted in the pink line in Fig. 7(b)]. Meanwhile, the combination (1) exhibits the largest vertical error [as shown in the brown line in Fig. 7(b)]. These experimental results are consistent with the evaluation using the RMSE of ICPs, as described previously.

a) Comparisons with other calibration methods: The performance of semi-OTJSC with combination (2) was also compared with the other three calibration methods (OTJSC, PC1-indoor, and PC2-outdoor). Their performances were assessed by analyzing the remaining systematic errors (image residuals) after the camera calibration process and the vertical error after AT process.

Image residuals: After SCBA, an incomplete lens distortion corrections will lead to systematic image residuals in the image plane, then introduce inaccurate EOPs and deform the
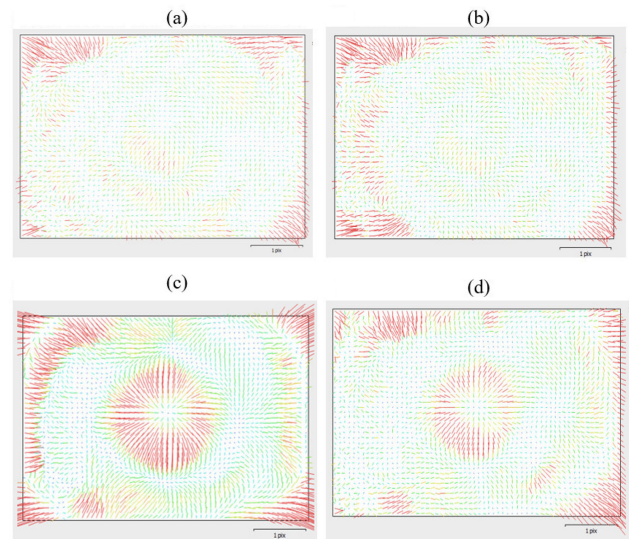

Fig. 8. Image residual plots across the sensor area of four camera calibration methods. (a) Semi-OTJSC with combination (2). (b) OTJSC. (c) PC1-indoor. (d) PC2-outdoor. The magnification factor is 1445. The scale bar outside the figure represents one pixel with a camera pixel size of 4.53 μm. The residual vectors from the smallest to the largest are denoted as blue, green, yellow, and red colors.

reconstructed 3-D model in the object space [57]. The "image residuals" represents the image coordinates difference of a 3-D feature reprojected to the image plane using the calibrated EOPs/IOPs/APs and compared with its image coordinates observation obtained by tie-point matching. Thus, the "image residuals plot" can illustrate the average reprojection error vectors for all pixels within the image frame [58]. The error budget of "reprojection error" includes the used camera calibration model, the adopted tie-point matching algorithm, image quality, tie-points distribution, accuracy and distribution of GCPs, the adjusted EOPs/IOPs/APs, as well as the image network and corresponding calibration method/procedure.
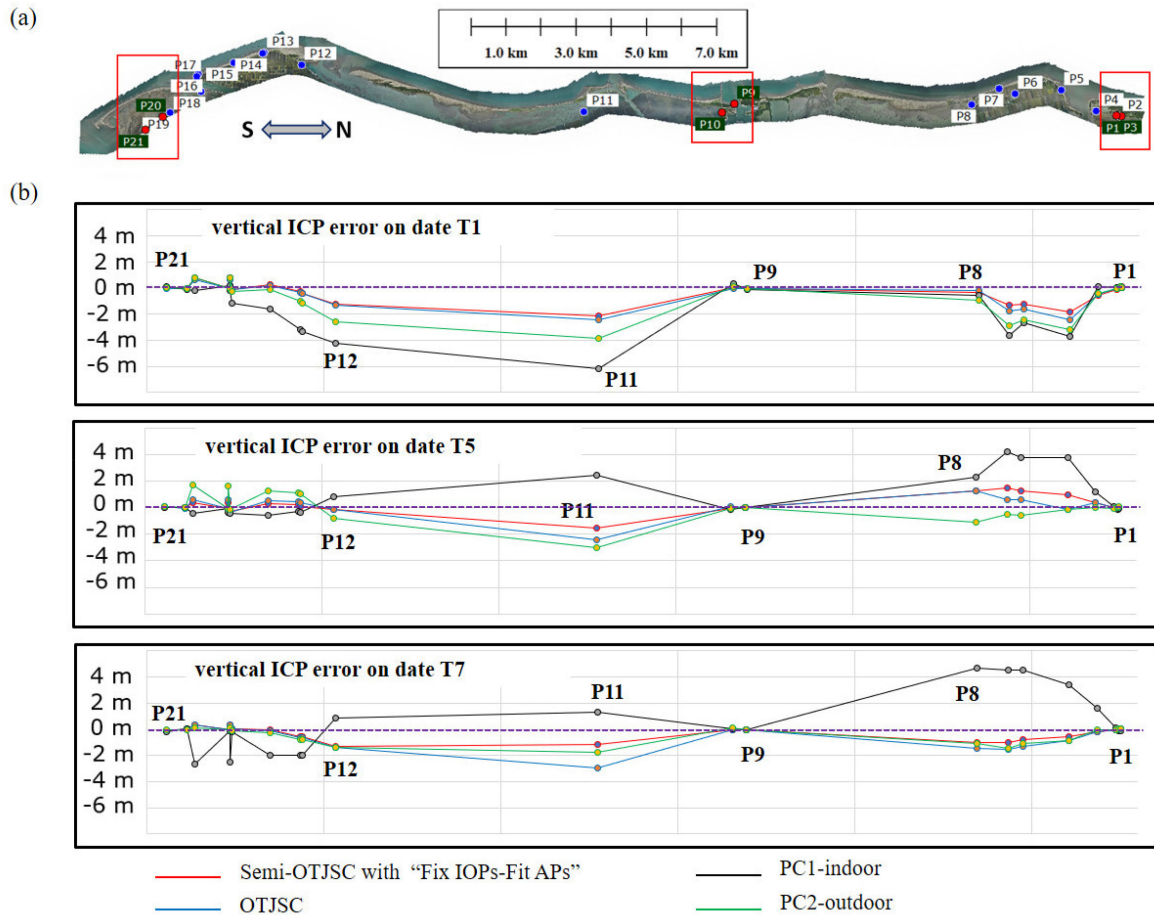
Fig. 9. Vertical ICP error of the un-even spatial control points distribution. (a) Uneven spatial control points distribution (each of the two GCPs was marked at the southern, center, and northern parts inside red rectangles). (b) Evaluation of four calibration methods through vertical ICP error on dates of T1, T5, and T7.

In this section, we investigate the ability of four calibration methods, i.e., semi-OTJSC with combination (2), OTJSC, PC1-indoor, and PC2-outdoor, to correct the lens distortions by performing AT process in T1 dataset. Fig. 8 illustrates image residuals plots for these four calibration methods. By visual inspection, the image residuals after calibration still hold small systematic errors, especially in PC1-indoor [see Fig. 8(c)] and PC2-outdoor [see Fig. 8(d)]. A harmonic trend can be seen in each plot. However, these systematic errors have been diminished significantly through the "semi-OTJSC with combination (2) Fix IOPs-Fit APs" approach, as shown in Fig. 8(a). As for the OTJSC method i.e., Fig. 8(b), the image residuals are all small. However, there are still some relatively larger residuals at the edge of sensor, as shown in red vectors of Fig. 8(b). In the meantime, the reasons cause larger errors in PC1-indoor and PC2-outdoor is probably due to the fact that the images were acquired at close range, which is different to the configuration of UAV images acquisition.

Vertical discrepancies: It is noticed that although the proposed camera calibration results can achieve the best-fit calibration method over the eight time-series datasets, a small systematical error undeniably exists. Since the geometrical accuracy of photogrammetric BA is strongly dependent on the number of GCPs and their distribution, we conduct an experiment to evaluate the vertical ICPs error after AT. A total of 21 points are used along the 30-km corridor mapping length, of which 6 points are GCPs and the remaining 15 points are ICPs [the GCPs distribution is depicted in the red rectangles of Fig. 9(a)]. This simulation was only conducted in three datasets: T1, T5, and T7. In the meantime, previous four camera calibration results were treated as precalibration data during the simulation.

As seen in Fig. 9(b), the configuration of the uneven spatial distribution leads to systematical vertical error ranging from −6 to 4 m among four camera calibration results. The errors dramatically increased and culminated in the areas without GCPs [corresponding to P8, P11, and P12 in Fig. 9(b)]—i.e., between two GCP regions. A similar error might occur at the sandbank areas because of the absence of GCPs (see Fig. 2). This demonstrates that the uneven spatial distribution of GCPs over a corridor area is a weak imaging geometry; thus, small systematic image residuals will propagate the errors during the estimation of EOPs.

According to the results, the "semi-OTJSC with combination (2)" obtained the smallest vertical RMS error of ICPs (0.84 m). In contrast, the PC1-indoor method has the highest error (2.55 m), indicating the worse overall accuracy. Quantitatively, as shown in Table III, the "semi-OTJSC with a combination (2)" obtained the lowest average vertical RMSE.

TABLE III
VERTICAL RMSES OF FOUR CAMERA CALIBRATION METHODS

Camera calibration methods	RMSE (m)			Average
	T1	T5	T7	
The proposed calibration strategy: semi-OTJSC with combination (2)	1.01	0.82	0.71	0.84
OTJSC by using images from sandbank UAV mapping	1.22	0.75	1.12	1.03
PC1-indoor	2.86	2.08	2.73	2.55
PC2-outdoor	1.89	1.27	0.86	1.34

TABLE IV
COMPARISONS OF THE SFM-MVS RESULTS BEFORE AND AFTER APPLYING CLAHE

	Dataset: Images within T8		Dataset: Images between T5 and T6 datasets	
	Original images	Enhanced images	Original images	Enhanced images
Detected key-points	451	596	618	689
Un-reliable tie-points	53	45	496	529
Percentage of un-reliable tie-points (%)	12	8	80	77
Valid tie-points	398	551	122	160
Percentage of increased tie-points after CLAHE (%)	38.4		31.1	

b) Summary: Through the above analyses, the best-fit calibration method [semi-OTJSC with a combination (2)] for the entire datasets can be obtained. This means that the focal length and principal point offset of the used camera are more stable over time. However, it may differ depending on the used lens/camera on the UAV mission. These results are in accordance with our treatment of the used camera/lens (i.e., always using the same lens and camera on every UAV mission, fixing the focusing rings with tape, never disassembling the lens from the camera body over the multitemporal applications, and turning off any feature settings that counteract the photogrammetric principles such as autofocusing).

It also reveals that precalibrating the IOPs using multiple altitudes UAV images together with high accuracy geotag information then followed by another calibration of APs through OTJSC is preferable. To conclude, among the four camera calibration methods, the suggested "semi-OTJSC with a combination (2)" approach obtains the smallest lens distortion residuals as well as the smallest vertical RMSE of ICPs (0.84 m). This contributes to reducing the vertical error by 19 cm compared to the OTJSC results, which have an average vertical RMSE of 1.03 m (see Table III). Therefore, this camera calibration result is used as the precalibration data in the Trans-AT co-registration process for the purpose of multitemporal morphological sandbanks analysis.

B. CLAHE Enhancement

The CLAHE enhancement was applied to the entire UAV sandbank images. The original colors are depicted in Fig. 10(a), as the samples of the original images of the dates of T1–T8. As expected, CLAHE algorithm demonstrates that the enhanced images exhibit a higher contrast and sharpness, thus improving the visualization effect of the original texture [see Fig. 10(b)]. The higher contrast and sharpness imply that the enhanced images have a higher visual quality and make the vague features of the image more visible. Subsequently, the enhanced images were used as the input data in the Trans-AT co-registration resulting in co-registered 3-D sparse clouds.

The performance of the CLAHE enhancement was then analyzed based on the number of valid and reliable tie-points (as shown in Table IV) in several images within the T8 datasets and between T5 and T6 datasets (which have the longest time interval, i.e., 225 days). These valid tie-points were obtained by eliminating those which were considered as unreliable and erroneous in a 3-D space. They were conducted through three-criterion tie-points filtering process, i.e., reconstruction uncertainty (due to poor geometry), projection accuracy (due to pixel matching errors), and reprojection error (pixel residual error). Those three procedures will eliminate unreliable and inaccurate tie-points in the sparse point clouds and will maintain the AT accuracies and subsequent dense point cloud generation. Therefore, for accurate point cloud generation purposes, before MVS process, we have to perform those three-criterion filtering processes for the entire datasets.

Fig. 10(c) and (d) illustrate how CLAHE can generally increase the number of detected feature points, thereby increasing the number of valid tie-points (the blue lines). The percentage of the increased tie-points within the images at the same epoch (T8) is 38.4% (see Table IV). At the same time, the CLAHE also reduces the percentage of the unreliable tie-points (i.e., 8%, compared to the original one with 12%). The percentage of the increased tie-points between two epochs in T5 and T6 also increases 31.1% (see Table IV). However, the quality of bundle adjustment results does not depend only on the number of extracted valid tie points, but it is highly affected by their correctness and distribution [59]. High precision and well spatial distribution of the extracted tie-points inhibit reliable estimation of the camera relative orientations. Here, we evident that using the enhanced images can provide better spatial tie-points distribution than the original one [as shown in blue dots in Fig. 10(e)].

Moreover, the generated DSM of the enhanced images has higher accuracy (closer to the VBS-RTK measurement) than the original ones with the vertical RMSEs of 23 and 34 cm, respectively [the comparison of the surface profiles are depicted in Fig. 10(f)]. This result shows that the use of enhanced images can improve the reliability and accuracy on the SfM process and diminish the vertical error by approximately 11 cm.

C. Trans-AT Co-Registration

In order to perform the coordinates transformation and co-registration of time-series UAV datasets, well spatial distributed GCPs are required. In this work, we marked 31 points (20 GCPs
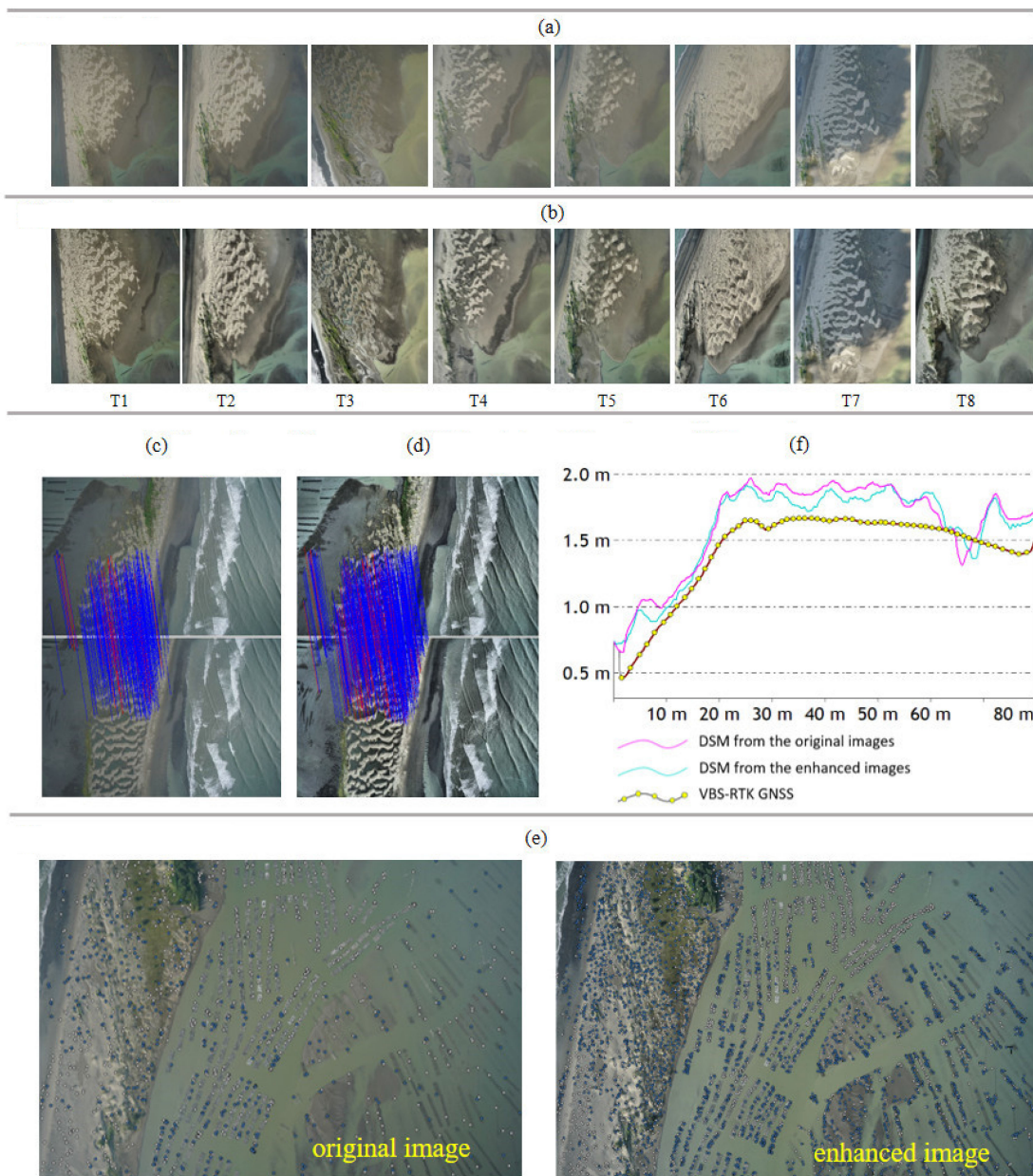
Fig. 10. Sample of the original images for T1–T8. (b) Enhanced images with CLAHE applied. It exhibits a higher visual quality, contrast, and brightness compared to the original images. (c) Tie-points matching between two original images and (d) the enhanced ones. The valid tie-points matching depicted as blue lines, whereas invalid depicted as red lines. (e) Surface profiles comparison between VBS-RTK measurements and DSMs profiles from the original image and the enhanced ones. (f) Sample of tie-points distribution in one image frame of the original and the enhanced one.

and 11 ICPs). However, their distributions are not well distributed, as shown in Fig. 2. Moreover, the study area is a long corridor shape with weak imaging geometry. Therefore, even if the best-fit calibrated camera model with GCPs is applied, we are still unable to perform a proper co-registration of the produced surface models. Thus, in this study, we adopt the Trans-AT co-registration scheme. The performance of the Trans-AT co-registration was evaluated by interpolating several surface profiles from the generated DTM after applying the Trans-AT with the best-fit calibrated camera model and compared with the VBS-RTK measured ones. Before DTM generation, we applied random forest for noises point removal owing to a significant

number of noisy points were found in the generated dense point clouds.

1) Noise Removal of Point Clouds on Water Surface: An example of noises on the T1 dataset is illustrated in Fig. 11(a), which is rendered in a 3-D perspective view for the inspection of noisy points. In order to generate bare-sand DTMs, the nonsand objects need to be removed. Random forest was adopted to classify them into several classes. Three subsets of point clouds [as depicted in purple rectangles in Fig. 11(a)] were selected as the training data (the inset picture showed the trained point clouds data). Through those trained point clouds, a trained model was built and applied to the whole point clouds, the results
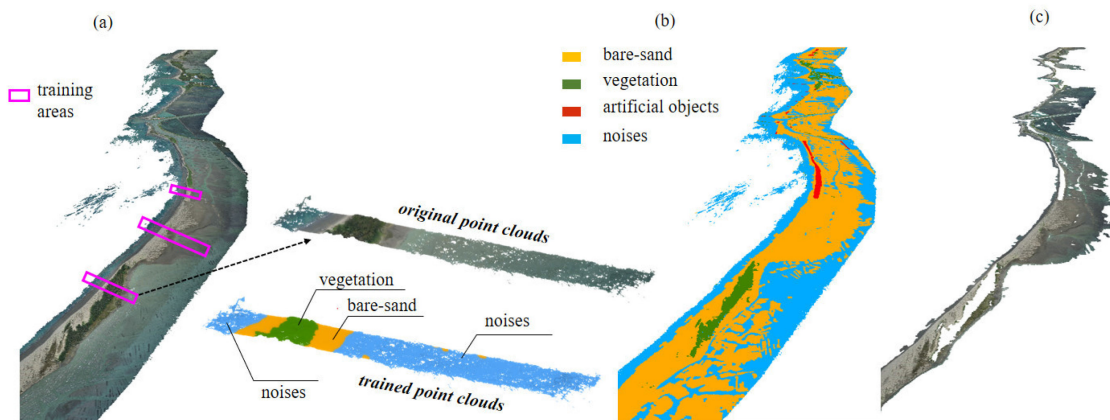
Fig. 11. Noises removal using random forest machine learning. (a) 3-D point clouds containing many noisy points. Point clouds inside purple rectangles were selected as training data. (b) Point clouds classification results. (c) Extracted bare-sand point clouds for DTM generation.

are illustrated in Fig. 11(b). They represent four classes of ground objects: bare-sand, trees, artificial objects, and noisy point clouds. In which, the bare-sand point clouds were mostly extracted [see Fig. 11(c)] and used for DTMs interpolation. The accuracy analysis of random forest approach for classifying bare-sand points (incorporates manual point clouds classification for validation) yielded the Kappa coefficient of 0.94.

2) Comparison With Other Co-Registration Strategies: For comprehensive assessment, the Trans-AT co-registration strategy was also compared with other two co-registration strategies (i.e., "Independent-AT with OTJSC" and "AT by joining multiepochs into a single block"). The surface profiles comparisons at three inland areas are depicted in Fig. 12(a) with the following findings:

1) Figures at the left column denote the surface profiles without applying the proposed strategy (i.e., independent-AT with OTJSC). This reflects that their AT process was conducted individually at each epoch with OTJSC. This procedure is commonly used for most UAV mapping projects. Based on the surface profiles among the eight datasets, this method has resulted in large variations in elevation. The elevation differences to the ground truth ranging from −38 to 66 cm, with an average of vertical RMSE of 26 cm [as depicted in blue triangles in Fig. 12(b)].

2) Figures on the right column present the surface profiles derived by means of "AT by joining multiepochs into a single block." It means that we combine all eight image datasets (i.e., a total of 7352 images) within a single block and perform AT together. Since the T6 images have PPK, their initial positions were assigned with a higher weight. We may find the overall elevation differences to the ground truth have been diminished significantly by applying this method, with an average of vertical RMSE of 13.5 cm [red dots in Fig. 12(b)]. However, this approach is impractical for multitemporal UAV missions. The whole co-registration process can be conducted only when the entire datasets were completely acquired. Moreover, the AT process among the entire datasets may fail because the objects may undergo significant change.

3) Figures at the central column depict the surface profiles generated by the proposed Trans-AT method. The results

have comparable achievements with the previous one. The overall elevation differences have diminished significantly (ranging from − 28 to 27 cm). The co-registrations among the eight datasets have more consistent surface trends. They are close to each other and yield the lowest discrepancy with an average vertical RMSE of 12.9 cm [green diamonds in Fig. 12(b)], which is close to 1 pixel of the image spatial resolution. Comparing with the previous method, the proposed Trans-AT method is more practical (i.e., the co-registration process can be conducted within two consecutive datasets).

Regarding the vertical accuracy, the surface profiles over the sand surface are more evident to evaluate the co-registration results owing to the absence of GCPs and relatively less texture over the sand areas. To confirm this aspect, the VBS-RTK measurement over sand surface was used. As shown in the blue line of Fig. 12(c), the surface profiles without applying the proposed method have resulted in a large elevation difference with a vertical RMSE of 46 cm. In contrary, through the "Trans-AT co-registration," as shown in green line of Fig. 12(c), its surface profile is closer to the ground truth. In addition, its vertical RMSE has significantly reduced to 17.2 cm.

This result is one of the major achievements for this study, even though most datasets do not contain PPK and well-distributed GCPs over a corridor area of 30×1 km. In the meantime, the surface profile of the "AT by joining multiepochs into a single block" method also obtains a closer result to the ground truth with a vertical RMSE of 19.4 cm. However, this method is not suggested, as it is impractical to multitemporal UAV mapping applications. To evaluate the final co-registration performance, we validate the significant difference of elevation between the interpolated surface profiles from DSMs generated after Trans-AT and VBS-RTK measurement at three inland areas.

Because those three inland areas were considered as unchanged, their elevation differences among the entire datasets should be close to zero. According to the validation results (see Table V), it yields a mean elevation difference of 9 cm, with the standard deviations (σ) of elevation differences in the range between 6 and 10.4 cm. We then ensure these significant elevation differences by the Student's *t*-test using (1). According to the test results, using a z-table with a confidence level of 95%,
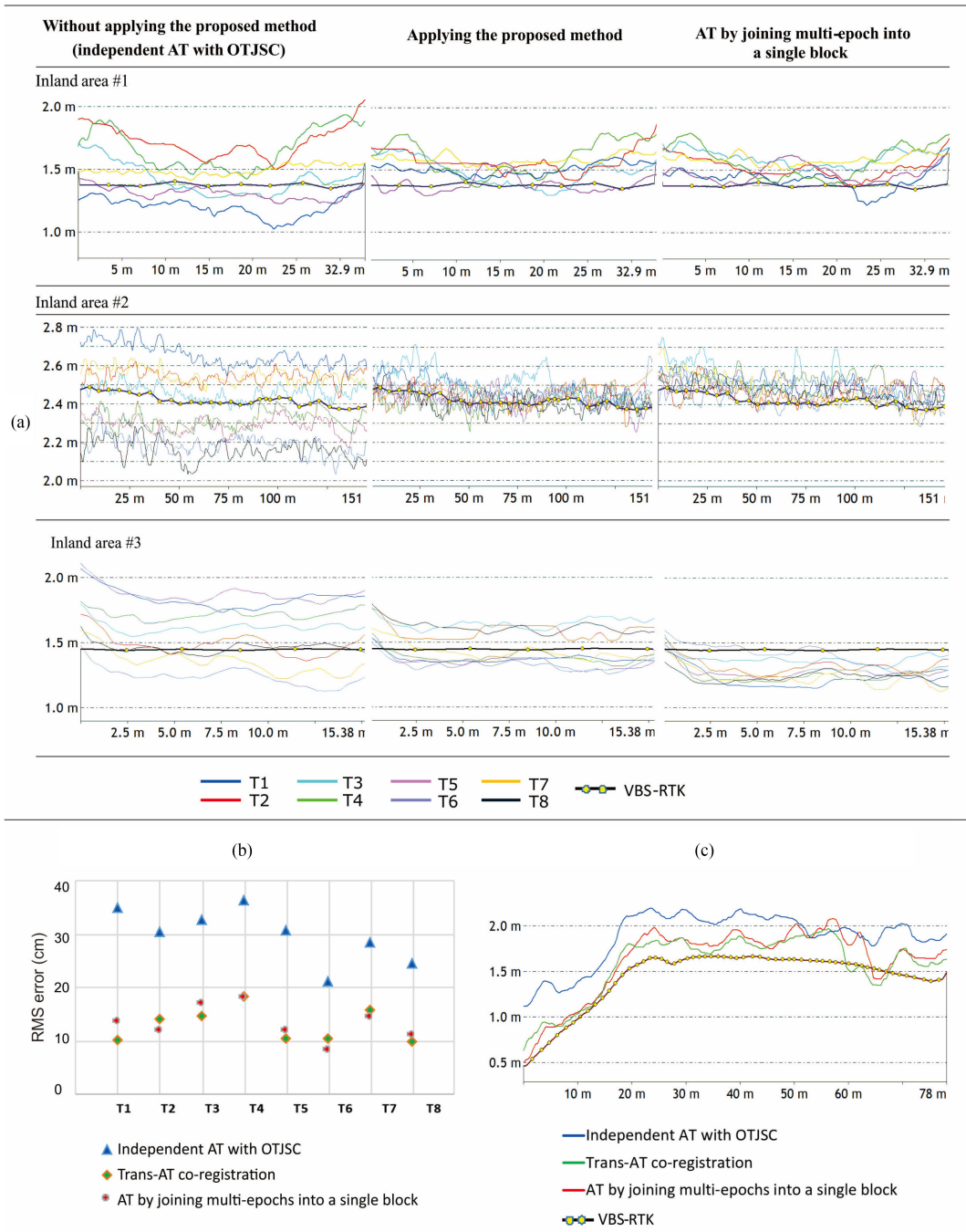
Fig. 12. (a) Comparisons of surface profiles at three inland areas from the proposed method with other two co-registration methods. Different colors denote different epochs, while the black one is the ground truth. (b) Vertical RMSEs of three co-registration strategies from three surface profiles at inland area. (c) Sand area surface profiles comparisons among the generated DTMs by three co-registration methods and the one measured by VBS-RTK (applied to T8 dataset).

the t_{value} of the significant difference test for all epochs were less than a t_{table} of 1.96 (see Table V), which confirms that the elevation differences among eight datasets are statistically "no significant change." These results highlight the successf of the suggested Trans-AT method without any significant elevation difference over the unchanged areas.

In fact, the success of the Trans-AT co-registration is highly dependent on the image initial positional accuracy of the reference dataset. In a multitemporal UAV mapping mission, it is necessary to acquire at least one epoch with high accuracy initial

positions (i.e., T6 with PPK) in order to maintain the trajectories of the other epochs and avoid the deformation of the generated surface models. It is because during the Trans-AT, two flights of UAV images datasets were constrained by means of tie-points. If the initial positions of the reference epoch were fixed, then the target images' positions and orientations can be maintained based on the derived relative orientations.

We further investigated the overall accuracy of seven steps Trans-AT without involving PPK geotagged information in the T6 dataset. These results in vertical RMSEs range from 60 to

TABLE V
STATISTICS OF ELEVATION DIFFERENCE AND CORRESPONDING SIGNIFICANT DIFFERENCE TEST RESULTS

|	T1	T2	T3	T4	T5	T6	T7	T8	Average
Standard deviation (σ) of elevation difference (at inland areas) (cm)	6.0	9.6	8.5	10.4	4.6	7.0	10.0	7.3	7.9
Mean of elevation difference ($\overline{\Delta z}$) (cm)	8.1	10.1	11.7	10.0	5.8	7.6	11.9	6.7	9.0
Vertical RMSE at inland areas (cm)	10.1	14.0	14.5	18.3	10.3	10.4	15.6	9.9	12.9
Vertical RMSE at sand area (cm)	-	-	-	-	-	-	-	17.2	17.2
t_{value} of significant difference test	1.35	1.06	1.37	0.96	1.26	1.09	1.19	0.91	
Significant difference test results				no significant change					
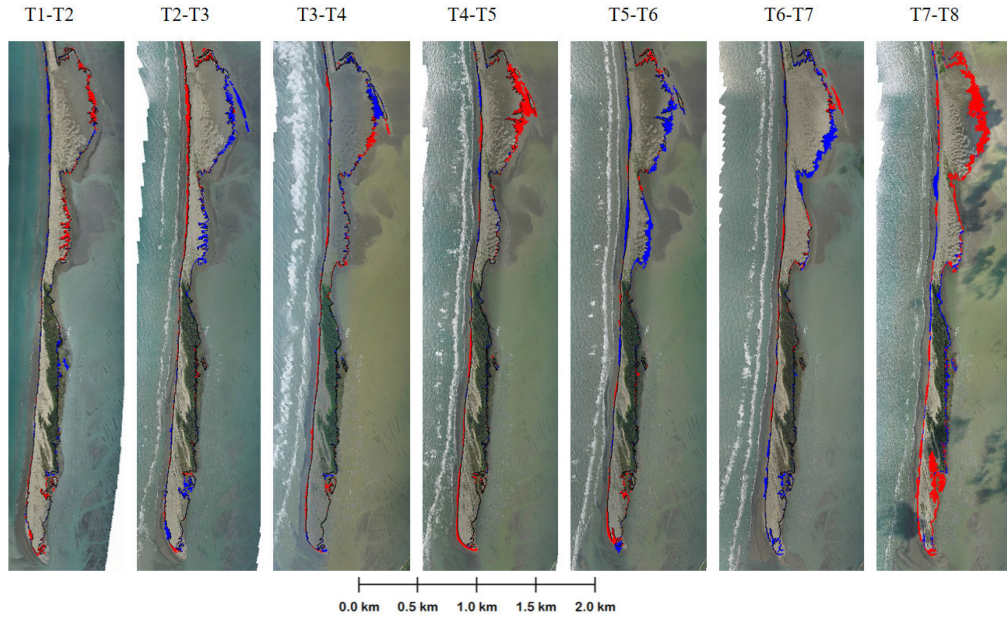
Fig. 13.   Mapped of lateral displacements between two consecutive sediment boundaries.

200 cm. It demonstrates the importance of image geolocation accuracy of the reference dataset, particularly in a corridor mapping application with weak imaging geometry and uneven GCPs distribution.

Through the Trans-AT co-registration, the high geolocation accuracy in reference dataset can be used to constrain the flight trajectories of the following epochs, it yields an average vertical RMSE of 12.9 cm (see Table V). Although a similar AT strategy was already proposed by Aicardi *et al.* [29] and Li *et al.* [60], the further steps of constraining the later datasets—by transferring the adjusted positions of the earlier datasets to the next ones, which is the next SIB—have never been explored yet, particularly its feasibility and stability. These further steps allow the latest dataset to be the "aerial control" to constrain the AT for the newest data collection. Its benefit is to minimize the feature matching failures within a SIB caused by significant object changes. Overall, these findings made the most significant contribution to the co-registration process among the time-series datasets in the corridor UAV mapping missions.

D. Sandbank Changes Analysis

The most common way to perform changes analysis is by calculating the DTM difference between any two epochs to support further quantitative analysis about the changes in geometric shape and depth. Here, we express the sandbank changes with two representations, i.e., planimetric lateral displacements (erosions and depositions) and changes in morphology. We have carried out these changes analysis only at the Cigu sandbank due to the limitation of paper length.

1) Lateral Erosions and Depositions: A coastal sandbank can suffer large erosions, mainly caused by storm waves [61]. The sand deposited at the sand foot is usually removed under breaking waves and then it migrates and deposits in the seaward direction. In the meantime, an intense storm can cause episodic erosion of a beach/sandbank system. However, the coastal system is generally recovered naturally by retrieving the sediment without human intervention [62], [63]. We have investigated these natural phenomena according to the sandbank boundaries extracted from the DTMs in the same contour lines. Based on the results, the lateral erosions mainly occurred between the dates of "T4–T5" and "T7–T8" as depicted in the red regions in Fig. 13. Meanwhile, the dominated lateral depositions correspond to the dates of "T5–T6" and "T6–T7," as depicted in the blue regions in Fig. 13.

2) Changes in Morphology: The morphological changes were assessed by using the generated DTMs and their differences. Fig. 14 provides the spatial information of the DTMs
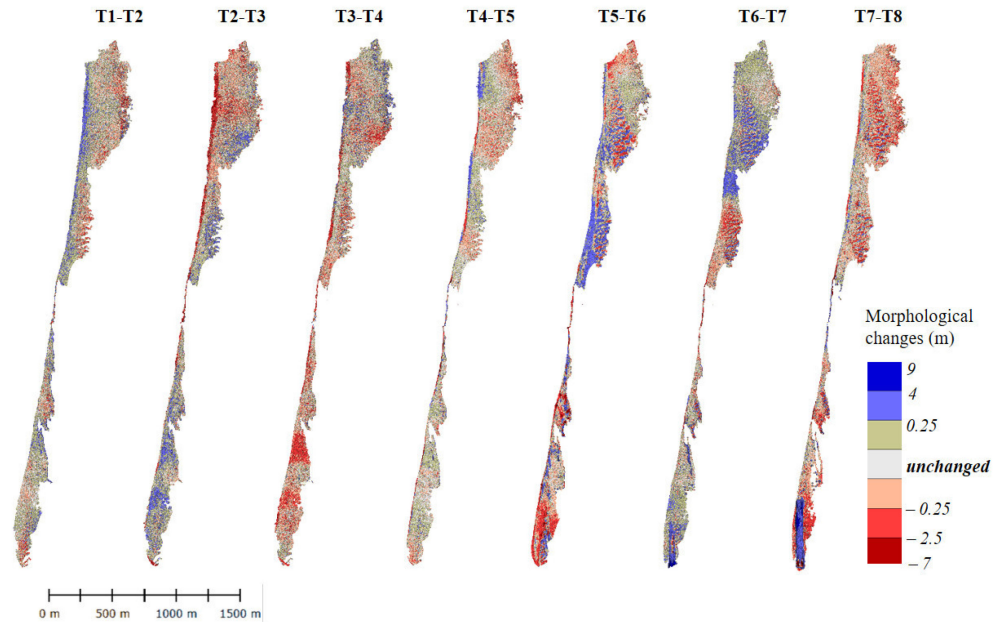
Fig. 14.   Changes in morphology between two consecutive DTMs at Cigu sandbank, exhibiting mapped of sediment redistribution of deposition or undergoing erosion.

differences. This information reveals the vertical depth and morphological changes that illustrate the sediment redistribution of deposition or undergoing erosion. The light green to blue indicates the sediment redistribution of depositions, while the light red to dark red denotes the erosions. Meanwhile, the grey areas indicate unchanged areas.

IV. Conclusion

A method for co-registering multitemporal UAV images with incomplete in-flight positions by PPK and uneven-distributed GCPs over a corridor-shaped area is proposed. To overcome the problems in the geometric distortion of image network, high image matching uncertainty, and high DTMs discrepancies in the co-registered products, two improvements are proposed in this study. First, the semi-OTJSC is suggested concerning the fact that the commonly used calibration procedure (i.e., on-the-job self-calibration) typically will not derive an appropriate lens distortion model in a long corridor area with flat terrain. Second, the Trans-AT co-registration procedure is introduced to minimize the geometric misalignment of multi-temporal surface models by means of GNSS-supported AT framework. In the meantime, CLAHE is applied to enhance the images before SCBA, thereby increasing the number of reliable tie-points within and between epochs datasets.

The experimental results indicate that the proposed semi-OTJSC camera calibration method with parameter-fitting combination of "Fix IOPs-Fit APs" can obtain the most stable camera model over the entire datasets. Comparing with purely OTJSC method, the calibrated camera model can decrease the vertical error by 19 cm. It reveals that the IOPs can be fixed during the co-registration of eight time-series datasets. However, our results demonstrate that the APs of the used camera/lens are not

stable over time. Thus, update of APs by OTJSC and evaluate a suitable parameter-fitting combination is suggested.

Enhancing the visual image quality through the CLAHE algorithm contributed to improve the reliability of the matched tie-points as well as the strength of relative orientation. The use of enhanced images can minimize the vertical discrepancies of the generated DSMs with 11 cm, which is about 1 pixel of UAV image spatial resolution, when comparing with the use of the original images. The suggested calibration method and the CLAHE enhanced images were further incorporated into the SfM and Trans-AT co-registration procedures. It achieves high accuracy results, with an average of vertical RMSE of 12.9 cm among the eight datasets in the inland areas and 17.2 cm at sand area, which are both lower than 1.5 pixels of the UAV image spatial resolution.

Another co-registration method (i.e., AT by joining multi-epochs into a single block) has also shown high accuracy with vertical RMSE at inland and sand areas of 13.5 and 19.4 cm, respectively. However, this method is impractical due to requiring the time-series datasets ready before the SfM-MVS process, and sometimes may fail because the ground objects have significant changed over time.

We have proven that our method achieves high co-registration accuracy and stability over the eight time-series datasets. This study demonstrates that the proposed Trans-AT co-registration method improves the overall absolute accuracy and minimizes the deformation at the reconstructed DTMs. The reconstructed DTMs after the Trans-AT co-registration and noise points removal are successfully used for assessing the sandbank lateral displacements and morphological changes over eight time-series epochs. These changes analysis will be helpful for researchers and local authorities to control the sandbank landscape equilibrium and support further environmental

management. In addition, the proposed co-registration method could be applied to other corridor mapping applications at large geographic extents in other environments worldwide.

REFERENCES

[1] F. Mancini, M. Dubbini, M. Gattelli, F. Stecchi, S. Fabbri, and G. Gabbianelli, "Using unmanned aerial vehicles (UAV) for high-resolution reconstruction of topography: The structure from motion approach on coastal environments," *Remote Sens.*, vol. 5, no. 12, pp. 6880–6898, 2013.

[2] S. Pan, N. MacDonald, J. Williams, B. A. O'Connor, J. Nicholson, and A. M. Davies, "Modelling the hydrodynamics of offshore sandbanks," *Continental Shelf Res.*, vol. 27, no. 9, pp. 1264–1286, 2007.

[3] T. J. Dolphin, C. E. Vincent, C. Coughlan, and J. M. Rees, "Variability in sandbank behaviour at decadal and annual time-scales and implications for adjacent beaches," *J. Coastal Res.*, no. 50, pp. 731–737, 2007.

[4] C. H. Jen, S. J. Chyi, L. L. Hsiao, M. S. Wu, and H. F. Lei, "The changing of coastal landform at Chikou barrier island and lagoon coast, Tainan, southwestern Taiwan," in *Proc. EGU Gen. Assem. Conf.*, vol. 14, p. 10097–1286, 2012.

[5] J. A. Gonçalves and R. Henriques, "UAV photogrammetry for topographic monitoring of coastal areas," *ISPRS J. Photogramm.*, vol. 104, pp. 101–111, 2015.

[6] W. Fu, J. Ma, P. Chen, and F. Chen, "Remote sensing satellites for digital earth," in *Manual of Digital Earth*, H. Guo, M. F. Goodchild, and A. Annoni, Eds., Singapore: Springer, 2020, pp. 55–123.

[7] X. Zheng, Q. Huang, J. Wang, T. Wang, and G. Zhang, "Geometric accuracy evaluation of high-resolution satellite images based on Xianning test field," *Sensors (Basel)*, vol. 18, no. 7, Jul. 2018, Art. no. 2121.

[8] A. M. A. Mahmoud, E. Hussain, A. Novellino, P. Psimoulis, and S. Marsh, "Monitoring the dynamics of formby sand dunes using airborne LiDAR DTMs," *Remote Sens.*, vol. 13, no. 22, 2021, Art. no. 4665.

[9] T. A. Łabuz, "A review of field methods to survey coastal dunes—Experience based on research from South Baltic coast," *J. Coastal Conservation*, vol. 20, no. 2, pp. 175–190, 2016.

[10] A. Nahon, P. Molina, M. Blázquez, J. Simeon, S. Capo, and C. Ferrero, "Corridor mapping of sandy coastal foredunes with UAS photogrammetry and mobile laser scanning," *Remote Sens.*, vol. 11, no. 11, pp. 1352–1366, 2019.

[11] C. Fey, M. Rutzinger, V. Wichmann, C. Prager, M. Bremer, and C. Zangerl, "Deriving 3D displacement vectors from multi-temporal airborne laser scanning data for landslide activity analyses," *GIScience Remote Sens.*, vol. 52, no. 4, pp. 437–461, 2015.

[12] N. S. Anders, A. C. Seijmonsbergen, and W. Bouten, "Geomorphological change detection using object-based feature extraction from multi-temporal LiDAR data," *IEEE Geosci. Remote Sens. Lett.*, vol. 10, no. 6, pp. 1587–1591, Nov. 2013.

[13] J. Liao, J. Zhou, and W. Yang, "Comparing LiDAR and SfM digital surface models for three land cover types," *Open Geosci.*, vol. 13, no. 1, pp. 497–504, 2021.

[14] M. Rusnák, J. Sládek, A. Kidová, and M. Lehotský, "Template for high-resolution river landscape mapping using UAV technology," *Measurement*, vol. 115, pp. 139–151, 2018.

[15] R. Koschitzki, E. Schwalbe, M. Krohnert, C. Cardenas, and H. Maas, "Multi-temporal photogrammetric analysis to monitoring the river Las Minas, Punta Arenas, Chile," *IEEE Latin Amer. Trans.*, vol. 16, no. 9, pp. 2481–2489, Sep. 2018.

[16] D. Skarlatos and V. Vamvakousis, "Long corridor survey for high voltage power lines design using UAV," *ISPRS Int. Arch. Photogrammetry, Remote Sens. Spatial Inf. Sci.*, vol. XLII-2/W8, pp. 249–255, 2017.

[17] P. Letortu *et al.*, "Examining high-resolution survey methods for monitoring cliff erosion at an operational scale," *GIScience Remote Sens.*, vol. 55, no. 4, pp. 457–476, 2018.

[18] J.-S. R. Over *et al.*, "Processing coastal imagery with Agisoft Metashape Professional Edition, Version 1.6—Structure from motion workflow documentation," USGS, Reston, VA, USA, Open-File Rep. 2021–1039, 2021.

[19] N. T. Giang, J. M. Muller, E. Rupnik, C. Thom, and M. Pierrot-Deseilligny, "Second iteration of photogrammetric processing to refine image orientation with improved tie-points," *Sensors (Basel)*, vol. 18, no. 7, Jul. 2018, Art. no. 2150.

[20] X. Huang, X. Wan, and D. Peng, "Robust feature matching with spatial smoothness constraints," *Remote Sens.*, vol. 12, no. 19, pp. 3158–3178, 2020.

[21] M. R. James and S. Robson, "Mitigating systematic error in topographic models derived from UAV and ground-based image networks," *Earth Surf. Processes Landforms*, vol. 39, no. 10, pp. 1413–1420, 2014.

[22] M. Mazzoleni, P. Paron, A. Reali, D. Juizo, J. Manane, and L. Brandimarte, "Testing UAV-derived topography for hydraulic modelling in a tropical environment," *Natural Hazards*, vol. 103, no. 1, pp. 139–163, 2020.

[23] E. Ferrer-González, F. Agüera-Vega, F. Carvajal-Ramírez, and P. Martínez-Carricondo, "UAV photogrammetry accuracy assessment for corridor mapping based on the number and distribution of ground control points," *Remote Sens.*, vol. 12, no. 15, pp. 2447–2466, 2020.

[24] R. Wackrow and J. H. Chandler, "A convergent image configuration for DEM extraction that minimises the systematic effects caused by an inaccurate lens model," *Photogrammetric Rec.*, vol. 23, no. 121, pp. 6–18, 2008.

[25] D. Skarlatos, E. Procopiou, G. Stavrou, and M. Gregoriou, "Accuracy assessment of minimum control points for UAV photography and georeferencing," *Proc. SPIE*, vol. 8795, 2013, Art. no. 879514.

[26] M. Jaud, S. Passot, P. Allemand, N. L. Dantec, P. Grandjean, and C. Delacourt, "Suggestions to limit geometric distortions in the reconstruction of linear coastal landforms by SfM photogrammetry with photoscan and micmac for UAV surveys with restricted GCPs pattern," *Drones*, vol. 3, no. 1, 2018, Art. no. 2.

[27] H. Zhang, E. Aldana-Jague, F. Clapuyt, F. Wilken, V. Vanacker, and K. Oost, "Evaluating the potential of PPK direct georeferencing for UAV-SfM photogrammetry and precise topographic mapping," *Earth Surf. Dyn. Discuss.*, pp. 1–34, Jan. 28, 2019.

[28] D. Feurer and F. Vinatier, "Joining multi-epoch archival aerial images in a single SfM block allows 3-D change detection with almost exclusively image information," *ISPRS J. Photogramm.*, vol. 146, pp. 495–506, 2018.

[29] I. Aicardi, F. Nex, M. Gerke, and A. Lingua, "An image-based approach for the co-registration of multi-temporal UAV image datasets," *Remote Sens.*, vol. 8, no. 9, pp. 779–799, 2016.

[30] S. Zambanini, "Feature-based groupwise registration of historical aerial images to present-day ortho-photo maps," *Pattern Recognit.*, vol. 90, pp. 66–77, 2019.

[31] S. Nagarajan and T. Schenk, "Feature-based registration of historical aerial images by area minimization," *ISPRS J. Photogramm.*, vol. 116, pp. 15–23, 2016.

[32] C. Zhao and A. A. Goshtasby, "Registration of multitemporal aerial optical images using line features," *ISPRS J. Photogramm.*, vol. 117, pp. 149–160, 2016.

[33] P. J. Besl and N. D. McKay, "A method for registration of 3-D shapes," *IEEE Trans. Pattern Anal. Mach. Intell.*, vol. 14, no. 2, pp. 239–256, Feb. 1992.

[34] S. Bouaziz, A. Tagliasacchi, and M. Pauly, "Sparse iterative closest point," *Comput. Graph. Forum*, vol. 32, no. 5, pp. 113–123, 2013.

[35] K.-H. Bae and D. D. Lichti, "A method for automated registration of unorganised point clouds," *ISPRS J. Photogramm.*, vol. 63, no. 1, pp. 36–54, 2008.

[36] P. Burdziakowski, C. Specht, P. S. Dabrowski, M. Specht, O. Lewicka, and A. Makar, "Using UAV photogrammetry to analyse changes in the coastal zone based on the sopot tombolo (Salient) measurement project," *Sensors (Basel)*, vol. 20, no. 14, Jul. 2020, Art. no. 4000.

[37] A. A. Gebrehiwot and L. Hashemi-Beni, "Three-dimensional inundation mapping using UAV image segmentation and digital surface model," *ISPRS Int. J. Geo-Inf.*, vol. 10, no. 3, pp. 144–157, 2021.

[38] S. M. Pizer, R. E. Johnston, J. P. Ericksen, B. C. Yankaskas, and K. E. Muller, "Contrast-limited adaptive histogram equalization: Speed and effectiveness," in *Proc. 1st Conf. Visual. Biomed. Comput.*, May 1990, pp. 337–345.

[39] L. Breiman, "Random forests," *Mach. Learn.*, vol. 45, no. 1, pp. 5–32, 2001.

[40] J. Ma, X. Fan, S. X. Yang, X. Zhang, and X. Zhu, "Contrast limited adaptive histogram equalization based fusion for underwater image enhancement," *Int. J. Pattern Recognit. Artif. Intell.*, vol. 32, 2017, Art. no. 1854018.

[41] R. Andaru, J.-Y. Rau, D. K. Syahbana, A. S. Prayoga, and H. D. Purnamasari, "The use of UAV remote sensing for observing lava dome emplacement and areas of potential lahar hazards: An example from the 2017–2019 eruption crisis at Mount Agung in Bali," *J. Volcanol. Geothermal Res.*, vol. 415, pp. 107255–107276, 2021.

[42] S. Lee, J. Park, E. Choi, and D. Kim, "Factors influencing the accuracy of shallow snow depth measured using UAV-based photogrammetry," *Remote Sens.*, vol. 13, no. 4, pp. 828–847, 2021.

[43] A. Habib, I. Detchev, and E. Kwak, "Stability analysis for a multicamera photogrammetric system," *Sensors (Basel)*, vol. 14, no. 8, pp. 15084–15112, Aug. 2014.

[44] J. Y. Rau and P. C. Yeh, "A semi-automatic image-based close range 3D modeling pipeline using a multi-camera configuration," *Sensors (Basel)*, vol. 12, no. 8, pp. 11271–11293, 2012.

[45] M. R. James, G. Antoniazza, S. Robson, and S. N. Lane, "Mitigating systematic error in topographic models for geomorphic change detection: Accuracy, precision and considerations beyond off-nadir imagery," *Earth Surf. Processes Landforms*, vol. 45, no. 10, pp. 2251–2271, 2020.

[46] C. Fraser, "Camera calibration considerations for UAV photogrammetry," in *Proc. ISPRS Tech. Commission II Symp.*, Jun. 2018, pp. 1–74. [Online]. Available: https://www.isprs.org/tc2-symposium2018/#keynote

[47] F. Benassi *et al.*, "Testing accuracy and repeatability of UAV blocks oriented with GNSS-supported aerial triangulation," *Remote Sens.*, vol. 9, no. 2, pp. 172–195, 2017.

[48] Y. Zhou, E. Rupnik, C. Meynard, C. Thom, and M. Pierrot-Deseilligny, "Simulation and analysis of photogrammetric UAV image blocks—Influence of camera calibration error," *Remote Sens.*, vol. 12, no. 1, pp. 22–39, 2019.

[49] V.-E. Oniga, N. Pfeifer, and A.-M. Loghin, "3D Calibration test-field for digital cameras mounted on unmanned aerial systems (UAS)," *Remote Sens.*, vol. 10, no. 12, pp. 2017–2039, 2018.

[50] F. He, T. Zhou, W. Xiong, S. Hasheminnasab, and A. Habib, "Automated aerial triangulation for UAV-based mapping," *Remote Sens.*, vol. 10, no. 12, 2018, Art. no. 1952.

[51] T. Tumurbaatar and T. Kim, "Comparative study of relative-pose estimations from a monocular image sequence in computer vision and photogrammetry," *Sensors (Basel)*, vol. 19, no. 8, Apr. 2019, Art. no. 1905.

[52] G. Forlani, E. Dall'Asta, F. Diotri, U. M. D. Cella, R. Roncella, and M. Santise, "Quality assessment of DSMs produced from UAV flights georeferenced with on-board RTK positioning," *Remote Sens.*, vol. 10, no. 2, 2018, Art. no. 311.

[53] A. R. Benjamin, D. O'Brien, G. Barnes, B. E. Wilkinson, and W. Volkmann, "Improving data acquisition efficiency: Systematic accuracy evaluation of GNSS-Assisted aerial triangulation in UAS operations," *J. Surveying Eng.*, vol. 146, no. 1, pp. 05019006-1–05019006-15, 2020.

[54] J. Carrivick, M. Smith, and D. Quincey, *Structure From Motion in the Geosciences*. Oxford, U.K.: Wiley, 2016.

[55] C. D. Ghilani, *Adjustment Computations*. 6th ed. Hoboken, NJ, USA: Wiley, 2017, pp. 57–78.

[56] R. Williams, "DEMs of difference," in *Geomorphological Techniques*, vol. 2, S. J. Cook, L. E. Clarke, and J. M. Nield, Eds., London, U.K.: British Soc. Geomorphol., 2012, pp. 1–17.

[57] F. Menna, E. Nocerino, S. Ural, and A. Gruen, "Mitigating image residuals systematic patterns in underwater photogrammetry," *Int. Arch. Photogrammetry, Remote Sens. Spatial Inf. Sci.*, vol. XLIII-B2-2020, pp. 977–984, 2020.

[58] E. Sanz-Ablanedo, J. Chandler, J. Rodríguez-Pérez, and C. Ordóñez, "Accuracy of unmanned aerial vehicle (UAV) and SfM photogrammetry survey as a function of the number and location of ground control points used," *Remote Sens.*, vol. 10, no. 10, pp. 1606–1625, 2018.

[59] V. Mousavi, M. Varshosaz, and F. Remondino, "Evaluating tie points distribution, multiplicity and number on the accuracy of uav photogrammetry blocks," *Int. Arch. Photogrammetry, Remote Sens. Spatial Inf. Sci.*, vol. XLIII-B2-2021, pp. 39–46, 2021.

[60] W. Li, K. Sun, D. Li, T. Bai, and H. Sui, "A new approach to performing bundle adjustment for time series UAV images 3D building change detection," *Remote Sens.*, vol. 9, no. 6, 2017, Art. no. 625.

[61] P. Dissanayake, J. Brown, P. Wisse, and H. Karunarathna, "Effects of storm clustering on beach/dune evolution," *Mar. Geol.*, vol. 370, pp. 63–75, 2015.

[62] M. I. Vousdoukas, L. P. M. Almeida, and Ó. Ferreira, "Beach erosion and recovery during consecutive storms at a steep-sloping, meso-tidal beach," *Earth Surf. Processes Landforms*, vol. 37, no. 6, pp. 583–593, 2012.

[63] T. Scott *et al.*, "The extreme 2013/2014 winter storms: Beach recovery along the southwest coast of England," *Mar. Geol.*, vol. 382, pp. 224–241, 2016.

Ruli Andaru received the M.Eng. degree in geomatics engineering from Gadjah Mada University, Yogyakarta, Indonesia, in 2010. He is currently working toward the Ph.D. degree in geomatics engineering with the Geomatics Department, College of Engineering, National Cheng Kung University, Tainan, Taiwan.

He has been working as a Lecturer and a Researcher with the Geodetic Engineering Department, Gadjah Mada University, since 2007. His research interests include UAV photogrammetry and remote sensing applications with emphasis on 3-D modeling and monitoring morphological changes on landscape terrain and active volcanoes.

Jiann-Yeou Rau received the Ph.D. degree in civil engineering from National Central University (NCU), Taoyuan, Taiwan, in 2002.

He was with the Center for Space and Remote Sensing Research, NCU, as a Research Scientist. He is currently a Professor with the Department of Geomatics, National Cheng Kung University, Tainan, Taiwan. His research activities are mostly concentrated in the domain of digital photogrammetry and mobile mapping technology through different platforms, such as aircraft, UAV, and land vehicle. His research interests include sandbank monitoring and bridge inspection through UAV images, LOD-2 building modeling, 3-D modeling of close-range objects, and other UAV and LiDAR applications.

Dr. Rau is a member of the Chinese Society of Photogrammetry and Remote Sensing and of Image Processing and Pattern Recognition, Taiwan.

Laurence Zsu-Hsin Chuang received the Ph.D. degree in civil engineering from the Department of Civil Engineering of North Carolina State University, Raleigh, NC, USA, in 1992.

He was the Deputy Director with the Coastal Ocean Monitoring Center, National Cheng Kung University. He is currently an Associate Professor with the Institute of Ocean Technology and Marine Affairs, National Cheng Kung University, Tainan, Taiwan. His research activities are mostly concentrated in the domain of meteoceanic observation (systems integration, data quality control), radar monitoring, statistical analysis, system dynamics, marine tourism and recreation management, information management.

Chia-Hung Jen received the Ph.D. degree in geography from the National Taiwan University (NTU), Taipei, Taiwan, in 2006.

He was with the Geography Department, NTU, as a Teaching Assistant. He is currently an Associate Researcher with the Department of Geography, CDTL, National Kaohsiung Normal University, Kaohsiung, Taiwan. His research activities are mainly in the domain of physical and human geography and geomorphology. His research interests include coastal change monitoring by RTK-GPS survey, landslide change detection, mudstone slope characteristics and dynamic monitoring by using LiDAR scan, the risk of coastal cities under the threat of climate change.